

# Dating individual quasars with the He II proximity effect

Gábor Worseck,<sup>1</sup>★ Ilya S. Khrykin,<sup>2,3</sup> Joseph F. Hennawi,<sup>4,5</sup> J. Xavier Prochaska,<sup>6,3</sup>  
and Emanuele Paolo Farina<sup>7</sup>

<sup>1</sup>*Institut für Physik und Astronomie, Universität Potsdam, Karl-Liebknecht-Str. 24/25, D-14476 Potsdam, Germany*

<sup>2</sup>*Southern Federal University, Stachki Avenue 194, 344090, Rostov-on-Don, Russia*

<sup>3</sup>*Kavli Institute for the Physics and Mathematics of the Universe (WPI), UTIAS, The University of Tokyo, Kashiwa, Chiba 277-8583, Japan*

<sup>4</sup>*Department of Physics, University of California, Santa Barbara, CA 93106, USA*

<sup>5</sup>*Max-Planck-Institut für Astronomie, Königstuhl 17, D-69117 Heidelberg, Germany*

<sup>6</sup>*University of California - Santa Cruz, 1156 High St., Santa Cruz, CA, USA 95064*

<sup>7</sup>*Max Planck Institut für Astrophysik, Karl-Schwarzschild-Straße 1, D-85748, Garching bei München, Germany*

Accepted 2021 June 7. Received 2021 April 23; in original form 2021 January 4

## ABSTRACT

Constraints on the time-scales of quasar activity are key to understanding the formation and growth of supermassive black holes (SMBHs), quasar triggering mechanisms, and possible feedback effects on their host galaxies. However, observational estimates of this so-called quasar lifetime are highly uncertain ( $t_Q \sim 10^4\text{--}10^9$  yr), because most methods are indirect and involve many model-dependent assumptions. Direct evidence of earlier activity is gained from the higher ionization state of the intergalactic medium (IGM) in the quasar environs, observable as enhanced Ly $\alpha$  transmission in the so-called proximity zone. Due to the  $\sim 30$  Myr equilibration time-scale of He II in the  $z \sim 3$  IGM, the size of the He II proximity zone depends on the time the quasar had been active before our observation  $t_{\text{on}} \leq t_Q$ , enabling up to  $\pm 0.2$  dex precise measurements of individual quasar on-times that are comparable to the  $e$ -folding time-scale  $t_S \sim 44$  Myr of SMBH growth. Here we present the first statistical sample of 13 quasars whose accurate and precise systemic redshifts allow for measurements of sufficiently precise He II quasar proximity zone sizes between  $\approx 2$  and  $\approx 15$  proper Mpc from science-grade *Hubble Space Telescope* (HST) spectra. Comparing these sizes to predictions from cosmological hydrodynamical simulations post-processed with one-dimensional radiative transfer, we infer a broad range of quasar on-times from  $t_{\text{on}} \lesssim 1$  Myr to  $t_{\text{on}} > 30$  Myr that does not depend on quasar luminosity, black hole mass, or Eddington ratio. These results point to episodic quasar activity over a long duty cycle, but do not rule out substantial SMBH growth during phases of radiative inefficiency or obscuration.

**Key words:** intergalactic medium – quasars: absorption lines – quasars: general – quasars: supermassive black holes – dark ages, reionization, first stars

## 1 INTRODUCTION

Quasars<sup>1</sup> are the most powerful sources of radiation that have emitted at an almost sustained high luminosity during the short  $\lesssim 60$  yr time-frame accessible to modern astronomical observations (Schmidt 1963). Most likely they are powered by accretion of baryons onto SMBHs (e.g. Salpeter 1964; Lynden-Bell 1969; Rees 1984), and it is believed that past quasar phases are required to explain the  $M_{\text{BH}} = 10^9\text{--}10^{10} M_\odot$  SMBHs found in the centres of nearby quiescent bulge-dominated galaxies (Soltan 1982; Kormendy & Richstone 1995; Yu & Tremaine 2002; Kormendy & Ho 2013). In numerical models of galaxy and black hole co-evolution, SMBH growth is triggered by gas inflow from major galaxy mergers (e.g. Di Matteo et al. 2005; Springel et al. 2005; Hopkins et al. 2005a,b, 2006, 2008; Capelo et al. 2015; Steinborn et al. 2018) and/or secular disc instabilities

(e.g. Hopkins & Quataert 2010; Novak et al. 2011; Bournaud et al. 2011; Gabor & Bournaud 2013; Hopkins et al. 2016; Anglés-Alcázar et al. 2013, 2017, 2020), but the physical processes on the relevant scales (sub-pc to a few pc) are still not fully understood. In both scenarios, kinetic and thermal feedback from stars and the SMBH self-regulate SMBH growth and obscuration. Once enough gas has been expelled, the SMBH shines as a short-lived UV-bright quasar until feedback quenches SMBH growth, and potentially also the star formation in the host galaxy (e.g. Sanders et al. 1988; Di Matteo et al. 2005; Springel et al. 2005; Hopkins et al. 2005b, 2006).

Although these models successfully reproduce many observed properties of galaxies and quasars, it remains challenging for them to explain the prevalence of  $M_{\text{BH}} = 10^9\text{--}10^{10} M_\odot$  SMBHs in  $z_{\text{em}} \gtrsim 6$  quasars, i.e. only  $< 10^9$  yr after the Big Bang (Jiang et al. 2007; Kurk et al. 2007; Mortlock et al. 2011; Venemans et al. 2013; De Rosa et al. 2014; Wu et al. 2015; Mazzucchelli et al. 2017; Bañados et al. 2018; Shen et al. 2019; Wang et al. 2020; Yang et al. 2020). These early SMBHs require either quasi-continuous Eddington-limited accretion onto massive black hole seeds (Sijacki et al. 2009; Di Matteo et al. 2012; Johnson et al. 2013), super-Eddington accretion (Volonteri &

★ E-mail: gworseck@uni-potsdam.de

<sup>1</sup> Unless otherwise specified, we use the term “quasar” to refer to an unobscured accreting supermassive black hole that radiates at a substantial fraction of its Eddington luminosity.

Rees 2005; Pacucci et al. 2015; Inayoshi et al. 2016), or radiatively inefficient accretion in possibly obscured phases (Madau et al. 2014; Volonteri et al. 2015; Pacucci et al. 2015; Davies et al. 2019).

Constraining the characteristic time-scales governing quasar activity is key to understanding the existence of early SMBHs, quasar triggering mechanisms, and whether feedback from SMBH growth might quench black hole fuelling and star formation. There is a growing consensus from models of galaxy and black hole co-evolution that fuelling, feedback, and quenching are intimately intertwined, which conspire to produce episodic quasar activity on a wide range of time-scales ( $10^4$ – $10^8$  yr, e.g. Ciotti & Ostriker 2001; Di Matteo et al. 2005; Hopkins et al. 2005b, 2006; Hopkins & Hernquist 2009; Hopkins et al. 2016; Novak et al. 2011; Gabor & Bournaud 2013; Steinborn et al. 2018; Anglés-Alcázar et al. 2017, 2020), often with significant variability in the accretion rate down to the time resolution limit of the simulation (10–100 yr, e.g. Novak et al. 2011; Anglés-Alcázar et al. 2020). Such short-term changes in the accretion rate may explain why some quasars show strong variability in their luminosity and/or their emission lines on time-scales of days to decades (LaMassa et al. 2015; Runnoe et al. 2016; MacLeod et al. 2016; McElroy et al. 2016; Yang et al. 2018). However, for longer time-scales the constraints from observations are uncertain by several orders of magnitude (e.g. Martini 2004), because the methods (i) are necessarily more indirect, (ii) are sensitive to particular time-scales, (iii) often yield a population average, and (iv) involve many model-dependent assumptions.

Comparisons of the quasar number density to their host dark matter halo abundance inferred from quasar clustering studies constrain the quasar duty cycle  $t_{\text{dc}}$ , i.e. the total time over the age of the Universe that a galaxy hosts a quasar (Haiman & Hui 2001; Martini & Weinberg 2001). Due to varying assumptions on how quasars populate dark matter haloes applied to partially discrepant quasar clustering measurements at  $z_{\text{em}} \sim 2$ –4, the inferred quasar duty cycle spans a wide range  $10^6 \text{ yr} \lesssim t_{\text{dc}} \lesssim 10^9 \text{ yr}$ , and may depend on redshift and/or luminosity (Porciani et al. 2004; Croom et al. 2005; Adelberger & Steidel 2005; Shen et al. 2007; White et al. 2008, 2012; Eftekharzadeh et al. 2015). Alternatively, the quasar duty cycle can be estimated by extending the Soltan (1982) argument such that the quasar luminosity function traces the gas accretion history onto SMBHs in present-day early-type galaxies. For present-day  $M_{\text{BH}} > 10^9 M_{\odot}$  SMBHs that shone as quasars at their Eddington limit the inferred duty cycle is  $t_{\text{dc}} = (6\text{--}30) \times 10^7 \text{ yr}$  (Yu & Tremaine 2002; Marconi et al. 2004; Shankar et al. 2004). The quasar duty cycle is a population average that is insensitive to the duration of individual quasar episodes.

The time distribution of high-accretion events, often called the episodic quasar lifetime  $t_{\text{Q}}$ , can be predicted by current numerical models or observationally estimated based on light travel time arguments. It has been suggested that mismatches between the level of nuclear activity and the ionization conditions of gas in and around the host galaxies imply significant nuclear variability on time-scales  $t_{\text{Q}} \sim 0.1 \text{ Myr}$  (Schawinski et al. 2015; Sartori et al. 2016; Schirmer et al. 2016; Keel et al. 2017; Oppenheimer et al. 2018). However, such short quasar lifetimes cannot explain the existence of giant ( $\sim 400 \text{ kpc}$ ) Ly $\alpha$  nebulae around  $z_{\text{em}} \sim 2$ –3 quasars (Cantalupo et al. 2014; Hennawi et al. 2015; Cai et al. 2017; Arrigoni Battaia et al. 2018), which require sustained activity for a few Myr. Moreover, the measured equivalent widths of Ly $\alpha$  emitters, enhanced by quasar-powered fluorescence, suggest quasar lifetimes of 1–40 Myr depending on the emitter sample and the quasar opening angle (Adelberger et al. 2006; Cantalupo et al. 2012; Trainor & Steidel 2013; Borisova et al. 2016; Marino et al. 2018). However, due to geometric dilution of the quasar flux, luminous Ly $\alpha$  emitters at distances of

several Mpc are more likely to be powered intrinsically (Khrykin et al. 2016).

The quasar lifetime can also be constrained from the locally enhanced UV radiation field in the quasar vicinity, the so-called proximity effect, which manifests itself as a region of enhanced IGM Ly $\alpha$  transmission (e.g. Bajtlik et al. 1988; Scott et al. 2000; Dall’Aglio et al. 2008; Calverley et al. 2011). Because the IGM reacts to a change in the photoionization rate  $\Gamma$  within a finite equilibration time-scale  $t_{\text{eq}} \approx \Gamma^{-1}$ , the existence of the proximity effect implies that quasars had been emitting continuously for  $t_{\text{Q}} \gtrsim t_{\text{eq}}$  (e.g. Bajtlik et al. 1988). With an H I UV background photoionization rate  $\Gamma_{\text{H I}} \approx 10^{-12} \text{ s}^{-1}$  measured in the  $2 \lesssim z \lesssim 5$  H I Ly $\alpha$  forest (Becker & Bolton 2013) one obtains a weak lower limit  $t_{\text{Q}} \gtrsim 0.03 \text{ Myr}$  for the quasar population.

During and shortly after H I reionization at  $z \gtrsim 5.7$ , the low IGM H I Ly $\alpha$  transmission enables measurements of well-defined sizes of H I proximity zones around individual quasars (Fan et al. 2006; Carilli et al. 2010; Eilers et al. 2017). The observation of any particular quasar is only sensitive to the time the quasar had been active prior to our observation at a random point during its current luminous episode, henceforth called the on-time  $t_{\text{on}} \leq t_{\text{Q}}$ . From their very small proximity zones given their luminosity, Eilers et al. (2020) concluded that 5–10 per cent of all  $z_{\text{em}} \sim 6$  quasars had recently turned on ( $t_{\text{on}} \lesssim 0.1 \text{ Myr}$ ), which is also supported by a lack of extended Ly $\alpha$  emission around them (Farina et al. 2019). However, because H I quickly equilibrates after quasar turn-on,  $z_{\text{em}} \sim 6$  H I proximity zones are insensitive to turn-on times  $t_{\text{on}} > 0.1 \text{ Myr}$  unless the IGM was significantly neutral (Keating et al. 2015; Eilers et al. 2017, 2018; Davies et al. 2020).

Stronger limits on the quasar lifetime may be inferred from the transverse proximity effect of a foreground quasar in a background line of sight via the additional light travel time. This effect has not been unambiguously detected in the  $z \sim 2$ –3 H I Ly $\alpha$  forest due to overdense environments around quasar hosts, quasar obscuration, and the small quasar boost to the overall H I photoionization rate (e.g. Liske & Williger 2001; Croft 2004; Hennawi & Prochaska 2007; Kirkman & Tytler 2008; Prochaska et al. 2013, but see Gonçalves et al. 2008). The low UV background in the post-reionization IGM increases the chance to discover the transverse proximity effect in the H I ( $t_{\text{on}} > 11 \text{ Myr}$ , Gallerani et al. 2008) and the He II Ly $\alpha$  forest ( $t_{\text{on}} \gtrsim 10$ –25 Myr, Jakobsen et al. 2003; Worseck & Wisotzki 2006; Worseck et al. 2007; Schmidt et al. 2017), but frequent non-detections can either be explained by a young age ( $t_{\text{on}} < 10 \text{ Myr}$ ) or obscuration (Schmidt et al. 2018).

Direct estimates of prolonged quasar activity can be inferred from the line-of-sight He II proximity zones of  $z_{\text{em}} \approx 3$ –4 quasars at the tail end of the He II reionization epoch, thanks to the long He II equilibration time-scale  $t_{\text{eq}} \approx \Gamma_{\text{He II}}^{-1} \approx 30 \text{ Myr}$  (Khrykin et al. 2016). This is comparable to the  $e$ -folding time-scale of SMBH growth  $t_{\text{S}} \sim 44 \text{ Myr}$  (Salpeter 1964), and may offer unique constraints on the range of episodic quasar lifetimes in models of galaxy and black hole co-evolution. In Khrykin et al. (2019, hereafter Paper I) we introduced a new statistical Bayesian method to infer on-times of individual quasars from their He II proximity zones, accounting for the degeneracy between the initial ambient IGM He II fraction and the quasar on-time that had affected previous analyses (Syphers & Shull 2014; Zheng et al. 2015). Applying our method to six He II-transparent quasars<sup>2</sup> at  $z_{\text{em}} > 3.6$  we inferred 0.3 dex precise on-

<sup>2</sup> He II-transparent quasars are rare quasars with sufficient flux at He II Ly $\alpha$  to secure a science-grade (signal-to-noise ratio  $\gtrsim 3$ ) spectrum with *HST* (e.g. Worseck & Prochaska 2011; Syphers et al. 2012; Worseck et al. 2019).

times for two quasars ( $t_{\text{on}} \approx 0.6$  and  $5.8$  Myr, respectively), while the remaining quasars allowed just for a joint constraint of a short  $\sim 1$  Myr on-time due to uncertainties in the quasar systemic redshifts.

Here we build on results from [Paper I](#), and apply a similar statistical algorithm to the sample of seventeen  $2.74 < z_{\text{em}} < 3.51$  He II-transparent quasars, twelve of which have accurate and precise systemic redshifts. In [Section 2](#) we describe our observations and the relevant parameters of our quasar sample. We present measurements of the He II proximity zone sizes in [Section 3](#). In [Section 4](#) we summarize our numerical model, before reporting on the inferred individual quasar on-times and their relation to quasar properties in [Section 5](#). We discuss our results and remaining uncertainties in [Section 6](#), before concluding in [Section 7](#).

We assume a flat  $\Lambda$ CDM cosmology with dimensionless Hubble constant  $h = 0.7$  ( $H_0 = 100h \text{ km s}^{-1} \text{ Mpc}^{-1}$ ), density parameters ( $\Omega_m, \Omega_b, \Omega_\Lambda$ ) = (0.27, 0.046, 0.73) for total matter, baryons, and cosmological constant, a linear dark matter power spectrum amplitude on a scale of  $8h^{-1}$  comoving Mpc  $\sigma_8 = 0.8$ , a spectral index of density perturbations  $n_s = 0.96$ , and a helium mass fraction  $Y = 0.24$ , consistent with [Planck Collaboration et al. \(2020\)](#). Proper distances are quoted explicitly in proper Mpc (pMpc).

## 2 OUR SPECTROSCOPIC DATA SET ON HE II PROXIMITY ZONES

### 2.1 HST/COS spectra of He II proximity zones

We use the *HST* UV spectra of seventeen out of twenty  $z_{\text{em}} < 3.6$  He II-transparent quasars from [Worseck et al. \(2019\)](#), to which we refer for a detailed description of the data reduction. Three  $z_{\text{em}} \approx 3$  quasars (HS 1157+3143, SDSS J0924+4852, SDSS J1101+1053) from [Worseck et al. \(2019\)](#) were excluded due to geocoronal H I Ly $\alpha$  contamination of the He II quasar proximity zone. For two  $z_{\text{em}} \approx 2.94$  quasars (SDSS J0818+4908, SDSS J0936+2927) we used only data taken in *HST*'s orbital shadow to exclude contamination of their He II proximity zones by geocoronal N I  $\lambda 1200 \text{ \AA}$  emission, as discussed in [Worseck et al. \(2019\)](#). Likewise, geocoronal O I was excluded for four  $z_{\text{em}} \approx 3.28$  quasars (HE2QS J1706+5904, HE2QS J2149–0859, Q 0302–003, HE2QS J0233–0149). Although the sightline to HE2QS J1706+5904 is not suitable for studying intergalactic He II due to an optically thick H I Lyman limit system at  $z = 0.4040$  ([Worseck et al. 2019](#)), its He II proximity zone is not impacted. [Table 1](#) lists the relevant properties of our sample.

All 17 *HST* spectra were taken with the Cosmic Origins Spectrograph (COS; [Green et al. 2012](#)), employing the G140L grating (12 spectra) or the G130M grating (5 spectra). Their resolving power  $R = \lambda/\Delta\lambda$  varies with wavelength and with the spatial position on the detector. [Table 1](#) lists the appropriate values in the spectral range of interest. The spectra were rebinned to 2–3 pixels per resolution element ( $R < 3000$ :  $\approx 0.24 \text{ \AA pixel}^{-1}$ ,  $10000 \leq R \leq 15000$ :  $\approx 0.04 \text{ \AA pixel}^{-1}$ ,  $R > 15000$ :  $\approx 0.03 \text{ \AA pixel}^{-1}$ ), yielding a signal-to-noise ratio  $S/N=3\text{--}19$  in the quasar continuum immediately redward of the He II quasar proximity zone.

After correction for Galactic extinction, the spectra were normalized by power laws  $f_\lambda \propto \lambda^\beta$ , fitted to spectral regions without strong emission and absorption features, but accounting for identified partial H I Lyman limit breaks ([Worseck et al. 2019](#)). Since our sample lacks contemporaneous and continuous spectral coverage from the rest-frame extreme UV to the near UV, a detailed correction for cumulative H I Lyman continuum attenuation is not possible. As such, the fitted power laws with a typical range in slope  $-3 \lesssim \beta \lesssim -0.5$

do not represent the intrinsic quasar spectral energy distributions (SEDs). The typical continuum error of a few per cent does not affect our analysis. We do not account for quasar He II Ly $\alpha$  and metal emission that is difficult to predict in detail in quasar accretion disc models (e.g. [Syphers et al. 2011a](#); [Syphers & Shull 2013](#)). Only two quasars (SDSS J0936+2927 and SDSS J2346–0016) show such features, and they are sufficiently weak that they do not change our results. Likewise, contamination of the proximity zone by low-redshift H I Lyman series lines is expected to be weak compared to the He II Ly $\alpha$  absorption.

Together with the seven  $z_{\text{em}} > 3.6$  quasars discussed in [Paper I](#), we arrive at a total sample of 24 quasars with He II proximity zones ([Table 1](#)).

### 2.2 Ancillary optical and near-infrared spectra

#### 2.2.1 Near-infrared spectroscopy

We obtained near-infrared spectra of 14 quasars from our combined sample to accurately measure their redshifts from their near-UV and optical emission lines. We successfully observed ten quasars with the Triple Spectrograph (TripleSpec, wavelength coverage  $1.0\text{--}2.45 \text{ \mu m}$  at  $R \sim 2700$ ; [Herter et al. 2008](#)) at the 200-inch Hale Telescope at Palomar Observatory in several observing campaigns between April 2011 and August 2012. Results on SDSS J1319+5202 have been reported in [Paper I](#). The total exposure times ranged from 0.625 to 2.5 hours depending on the brightness of the target and the observing conditions. The TripleSpec spectra were reduced using a custom pipeline based on the LOWREDUX package<sup>3</sup> ([Prochaska & Hennawi 2009](#)). Wavelength solutions were computed from OH sky emission lines, and heliocentric corrections were applied. For all spectra, relative fluxing was performed with a telluric standard star observed close in time and in airmass to the science target. In the TripleSpec sample the  $S/N$  per  $91.4 \text{ km s}^{-1} \text{ pixel}$  ranges from 6 to 50 near the quasar emission lines of interest.

Near-infrared spectra of two further quasars were successfully obtained with the Large Binocular Telescope Utility Cameras in the Infrared 1 and 2 (LUCI1/2; [Seifert et al. 2003](#)) in January 2014. We used the N1.8 cameras in seeing-limited mode. HS 1024+1849 was observed for a total 20 minutes with the LUCI1 G200 grating in the wavelength range  $0.95\text{--}1.34 \text{ \mu m}$  and the  $0.5''$  slit ( $R \sim 2400$ ). HS 0911+4809 was observed for 20 minutes during LUCI2 commissioning with the G150 grating in the wavelength range  $2.02\text{--}2.28 \text{ \mu m}$  and the  $0.75''$  slit ( $R \sim 2700$ ). The LUCI data were reduced with a custom set of IRAF<sup>4</sup> routines. Each exposure was flat fielded and cleaned of cosmic ray hits using the procedure described in [van Dokkum \(2001\)](#). Wavelength calibration was achieved by matching the position of OH sky lines in the two-dimensional spectra, and sky subtraction was performed by subtracting subsequent pairs of frames that had been taken in a standard ABBA dithering pattern. Relative flux calibration and telluric correction of the extracted spectra was performed with A0V stars observed immediately after the science targets. In the wavelength range of interest the LUCI1 (LUCI2) spectrum of HS 1024+1849 (HS 0911+4809) reaches  $S/N=10$  ( $S/N=5$ ) per  $2.13 \text{ \AA}$  ( $2.67 \text{ \AA}$ ) pixel.

HE2QS J1630+0435 from [Paper I](#) was successfully observed with

<sup>3</sup> [www.ucolick.org/~xavier/LowRedux](http://www.ucolick.org/~xavier/LowRedux)

<sup>4</sup> IRAF ([Tody 1993](#)) is distributed by the National Optical Astronomy Observatory, which is operated by the Association of Universities for Research in Astronomy under a cooperative agreement with the National Science Foundation.



**Table 1.** Our combined sample of 24 quasars with He II proximity zones, comprising new measurements for 17  $z_{\text{em}} < 3.6$  quasars and results for seven  $z_{\text{em}} > 3.6$  quasars from Paper I. We list the name, position, *HST*/COS resolving power and signal-to-noise ratio near He II Ly $\alpha$  in the quasar rest frame, quasar redshift, velocity (redshift) uncertainty, emission line and instrument for redshift measurement, SDSS or Pan-STARRS *i* band magnitude corrected for Galactic extinction, absolute magnitude at 1450 Å rest frame, He II-ionizing photon production rate  $Q$ , measured proximity zone size  $R_{\text{pz}}$ , and inferred quasar on-time  $t_{\text{on}}$  for an assumed uniform prior on the He II fraction  $0.01 \leq x_{\text{He II},0} \leq 1$  (Section 5.2).

Quasar	R.A. (J2000)	Decl. (J2000)	$R$	S/N <sup>a</sup>	$z_{\text{em}}$	$\sigma_v$ km s <sup>-1</sup>	Line	Instrument	$m_i$ mag	$M_{1450}$ mag	$\log \frac{Q}{s^{-1}}$	$R_{\text{pz}}$ pMpc	$t_{\text{on}}$ Myr
HE 2347–4342	23 <sup>h</sup> 50 <sup>m</sup> 34 <sup>s</sup> .21	−43°25′59″.6	17000	19	2.8852	44.4	[O III]	FIRE	− <sup>b</sup>	−28.69 <sup>b</sup>	57.08	−4.77 ± 0.15	–
HE2QS J2149–0859	21 <sup>h</sup> 49 <sup>m</sup> 27 <sup>s</sup> .77	−08°59′03″.6	1700	3	3.2358	656	C IV	CAFOS	18.67	−26.83	56.34	−0.63 ± 2.04	< 0.46
HE2QS J1706+5904	17 <sup>h</sup> 06 <sup>m</sup> 21 <sup>s</sup> .74	+59°04′06″.4	1700	4	3.2518	656	C IV	CAFOS	18.86	−26.66	56.27	−0.04 ± 2.03	< 0.66
SDSS J1237+0126	12 <sup>h</sup> 37 <sup>m</sup> 48 <sup>s</sup> .99	+01°26′07″.0	2400	4	3.1467	273	Mg II	TripleSpec	18.78	−26.66	56.27	1.77 ± 0.87	< 1.01
SDSS J2346–0016	23 <sup>h</sup> 46 <sup>m</sup> 25 <sup>s</sup> .66	−00°16′00″.4	2600	8	3.5076	273	Mg II	TripleSpec	17.68	−27.97	56.79	2.66 ± 0.77	0.31 <sup>+0.41</sup> <sub>−0.21</sub>
SDSS J0818+4908	08 <sup>h</sup> 18 <sup>m</sup> 50 <sup>s</sup> .01	+49°08′17″.0	2200	4	2.9598	656	C IV	BOSS	18.36	−26.93	56.38	2.92 ± 2.25	< 2.42
HE2QS J0916+2408	09 <sup>h</sup> 16 <sup>m</sup> 20 <sup>s</sup> .85	+24°08′04″.6	1800	4	3.4231	656	C IV	CAFOS	18.52	−27.12	56.45	3.14 ± 1.91	< 2.77
HS 0911+4809	09 <sup>h</sup> 15 <sup>m</sup> 10 <sup>s</sup> .01	+47°56′58″.8	10000	6	3.3500	400	H $\beta$	LUCI2	17.77	−27.84	56.74	4.21 ± 1.19	1.01 <sup>+1.29</sup> <sub>−0.69</sub>
HE2QS J0233–0149	02 <sup>h</sup> 33 <sup>m</sup> 06 <sup>s</sup> .01	−01°49′50″.5	1700	4	3.3115	656	C IV	CAFOS	18.41	−27.17	56.47	4.71 ± 1.98	< 6.24
Q 1602+576	16 <sup>h</sup> 03 <sup>m</sup> 55 <sup>s</sup> .92	+57°30′54″.4	15000	7	2.8608	273	Mg II	TripleSpec	17.22	−27.99	56.80	6.10 ± 0.97	1.98 <sup>+1.41</sup> <sub>−0.94</sub>
PC 0058+0215	01 <sup>h</sup> 00 <sup>m</sup> 58 <sup>s</sup> .39	+02°31′31″.4	2200	4	2.8842	273	Mg II	TripleSpec	18.77	−26.46	56.19	7.10 ± 0.97	> 7.24
HS 1700+6416	17 <sup>h</sup> 01 <sup>m</sup> 00 <sup>s</sup> .61	+64°12′09″.1	2100	15	2.7472	273	Mg II	TripleSpec	15.79	−29.33	57.34	7.16 ± 1.01	0.80 <sup>+0.50</sup> <sub>−0.35</sub>
SDSS J0936+2927	09 <sup>h</sup> 36 <sup>m</sup> 43 <sup>s</sup> .50	+29°27′13″.6	2200	4	2.9248	44.4	[O III]	TripleSpec	18.06	−27.20	56.49	8.59 ± 0.15	11.62 <sup>+7.37</sup> <sub>−4.57</sub>
HS 1024+1849	10 <sup>h</sup> 27 <sup>m</sup> 34 <sup>s</sup> .13	+18°34′27″.5	15000	5	2.8521	273	Mg II	LUCI1	17.66	−27.54	56.62	9.38 ± 0.97	9.53 <sup>+6.83</sup> <sub>−4.08</sub>
SDSS J1253+6817	12 <sup>h</sup> 53 <sup>m</sup> 53 <sup>s</sup> .71	+68°17′14″.2	2600	7	3.4753	44.4	[O III]	TripleSpec	18.45	−27.19	56.48	11.40 ± 0.12	> 23.55
Q 0302–003	03 <sup>h</sup> 04 <sup>m</sup> 49 <sup>s</sup> .85	−00°08′13″.5	19000	3	3.2850	44.4	[O III]	TripleSpec	17.34	−28.21	56.89	13.20 ± 0.13	> 11.36
HE2QS J2157+2330	21 <sup>h</sup> 57 <sup>m</sup> 43 <sup>s</sup> .63	+23°30′37″.3	1600	4	3.1465	44.4	[O III]	TripleSpec	17.67	−27.77	56.72	17.40 ± 0.14	> 31.84
HE2QS J2354–2033 <sup>c</sup>	23 <sup>h</sup> 54 <sup>m</sup> 52 <sup>s</sup> .00	−20°33′20″.7	2300	3	3.7745	656	C IV	LRIS	18.90	−26.88	56.37	−3.65 ± 1.68	–
HE2QS J2311–1417 <sup>c</sup>	23 <sup>h</sup> 11 <sup>m</sup> 45 <sup>s</sup> .46	−14°17′52″.1	2300	4	3.7003	656	C IV	Kast	18.11	−27.64	56.66	1.94 ± 1.72	< 0.86
SDSS J1614+4859 <sup>c</sup>	16 <sup>h</sup> 14 <sup>m</sup> 26 <sup>s</sup> .81	+48°59′58″.8	2300	3	3.8175	656	C IV	BOSS	19.45	−26.34	56.14	2.72 ± 1.66	< 5.98
SDSS J1711+6052 <sup>c</sup>	17 <sup>h</sup> 11 <sup>m</sup> 34 <sup>s</sup> .41	+60°52′40″.3	2700	4	3.8358	656	C IV	SDSS	19.34	−26.49	56.19	2.97 ± 1.65	< 7.48
SDSS J1319+5202 <sup>c</sup>	13 <sup>h</sup> 19 <sup>m</sup> 14 <sup>s</sup> .20	+52°02′00″.1	2700	2	3.9166	400	H $\beta$	TripleSpec	17.81	−28.02	56.82	3.62 ± 0.98	0.80 <sup>+0.88</sup> <sub>−0.50</sub>
SDSS J1137+6237 <sup>c</sup>	11 <sup>h</sup> 37 <sup>m</sup> 21 <sup>s</sup> .72	+62°37′07″.2	2300	4	3.7886	656	C IV	BOSS	19.31	−26.46	56.19	4.92 ± 1.68	> 1.34
HE2QS J1630+0435 <sup>c</sup>	16 <sup>h</sup> 30 <sup>m</sup> 56 <sup>s</sup> .34	+04°35′59″.4	2000	4	3.8101	400	H $\beta$	ISAAC	17.51	−28.37	56.92	8.43 ± 1.02	2.77 <sup>+2.27</sup> <sub>−1.33</sub>

<sup>a</sup>Signal-to-noise ratio per pixel near He II Ly $\alpha$  ( $R < 3000$ :  $\approx 0.24 \text{ Å pixel}^{-1}$ ,  $10000 \leq R \leq 15000$ :  $\approx 0.04 \text{ Å pixel}^{-1}$ ,  $R > 15000$ :  $\approx 0.03 \text{ Å pixel}^{-1}$ ).

<sup>b</sup>For HE 2347–4342 we obtained the observed AB magnitude  $m_{1450} = 16.83$  from its VLT/FORS2 spectrum calibrated to  $B_{\text{Vega}} = 17.18$  (Worseck et al. 2008).

<sup>c</sup> $z_{\text{em}} > 3.6$  quasar reported in Paper I. The inferred  $t_{\text{on}}$  is based on the extended grid of radiative transfer models (Section 4.1) and our updated definition of upper and lower limits (Section 5.2).

the Very Large Telescope Infrared Spectrometer And Array Camera (ISAAC; Moorwood et al. 1998). We covered the wavelength range 2.31–2.43  $\mu\text{m}$  with the medium-resolution grating and the 0.6'' slit ( $R \sim 4400$ ) for a total exposure of 1.1 hours using standard AB dithering. The data were processed with the LOWREDUX package. The reduced spectrum reaches a  $S/N \approx 15$  per  $\approx 1.18 \text{ Å pixel}$ .

For the quasar HE 2347–4342 we use a reduced  $R \sim 3600$  spectrum taken with the Folded-port InfraRed Echelle (FIRE; Simcoe et al. 2008) spectrometer on the 6.5 m Magellan Baade Telescope, kindly provided by R. Simcoe (private communication). It reaches a  $S/N \approx 40$  per  $12.5 \text{ km s}^{-1}$  pixel in the wavelength range of interest.

## 2.2.2 Optical spectroscopy

The remaining ten quasars from our combined sample have only optical spectra available, which cover their rest-frame far-UV emission lines. For four quasars from Table 1 we use  $R \sim 200$  discovery spectra taken with Calar Alto Faint Object Spectrograph (CAFOS) at the Calar Alto 2.2 m telescope (Worseck et al. 2019). HE2QS J2311–1417 from Paper I had been discovered with the Kast spectrometer at the Lick 3 m Shane Telescope (Worseck et al. 2019). For HE2QS J2354–2033 from Paper I we employed a higher-quality follow-up spectrum taken with the Keck Low Resolution Imaging Spectrometer (LRIS; Oke et al. 1995; Steidel et al. 2004). For the remaining 4/24 quasars from our He II proximity zone sample that had been discovered in the Sloan Digital Sky Survey (SDSS; York et al. 2000) we retrieved their highest-quality spectra from SDSS Data Release 14 (Abolfathi et al. 2018), taken either with the original SDSS spectrograph or the Baryon Oscillation Spectroscopic Survey (BOSS) spectrograph (Smee et al. 2013).

For five quasars with small He II proximity zones we also dis-

cuss below medium- and high-resolution optical spectra of their H I proximity regions. We observed HS 0911+4809 with the Keck High-Resolution Echelle Spectrometer (HIRES; Vogt et al. 1994), using the C1 decker (0.86'' slit,  $R \sim 45,000$ ) and the red cross disperser. The combined reduced spectrum reaches a  $S/N \sim 60$  per  $2.6 \text{ km s}^{-1}$  pixel in the H I proximity region. SDSS J1319+5202 was observed with the Keck Echelle Spectrograph and Imager (ESI; Sheinis et al. 2002) using the 0.75'' slit ( $R \sim 5400$ ), yielding a  $S/N \sim 60$  per  $10 \text{ km s}^{-1}$  pixel. The H I proximity region of SDSS J1237+0126 was covered in an archival Keck/HIRES spectrum (O’Meara et al. 2015) at  $S/N \sim 20$  per  $2.6 \text{ km s}^{-1}$  pixel. The VLT and Keck spectra of HE 2347–4342 and SDSS J2346–0016 were taken from Worseck et al. (2016).

## 2.3 Redshift measurements

Quasar redshifts were determined from UV-optical quasar emission lines covered in the available optical and near-infrared spectra, accounting for their velocity shifts relative to systemic (traced by [O II] emission or Ca II absorption). The velocity shifts are due to bulk motions in the quasar broad line region, with high-ionization lines showing a strong dependence of the blueshift on the continuum luminosity (e.g. Gaskell 1982; Tytler & Fan 1992; Vanden Berk et al. 2001; Richards et al. 2002, 2011; Hewett & Wild 2010; Shen et al. 2016). We measured the mode of each emission line using the algorithm described in Hennawi et al. (2006), which accounts for line blending (in particular C IV  $\lambda 1549$  blended with He II  $\lambda 1640$ , and H $\beta$   $\lambda 4863$  blended with [O III]  $\lambda \lambda 4959, 5007$ ), and is robust against noise, line asymmetries, and associated absorption for the lines that were used eventually ( $S/N > 10$ ). Considering our typical  $S/N$  we fitted each emission line with a single Gaussian profile. The measured redshifts were corrected to the systemic frame by accounting

for their average blueshifts, and precisions were assigned from the standard deviations  $\sigma_v$  of the velocity distributions in large quasar samples (Richards et al. 2002; Boroson 2005; Richards et al. 2011; Shen et al. 2016). The redshift precision was our primary criterion for the eventually adopted emission line and redshift in Table 1:

(i) We preferred redshifts from detected narrow [O III]  $\lambda 5007$  emission ( $S/N > 10$  across the line, peak to continuum ratio  $> 0.3$ , 5 quasars in Table 1). We assumed a luminosity-independent blueshift of  $-27.1 \text{ km s}^{-1}$  w.r.t. the systemic frame defined by low-ionization forbidden lines ([O II], [N II], [S II]), and a velocity precision  $\sigma_v = 44.4 \text{ km s}^{-1}$ , both based on the high-confidence sample in Boroson (2005). The values are in good agreement with Hewett & Wild (2010) and Shen et al. (2016).

(ii) If [O III] was not covered or not detected due to low  $S/N$  or the Baldwin effect (e.g. Baldwin 1977; Stern & Laor 2012; Shen & Ho 2014; Shen 2016), we took broad Mg II if the line was detected at  $S/N > 10$  (6 quasars). We assumed the same luminosity-independent blueshift of  $-27.1 \text{ km s}^{-1}$  as for [O III], and a velocity precision  $\sigma_v = 273 \text{ km s}^{-1}$  derived by Gaussian error propagation of the [O III] velocity precision ( $44.4 \text{ km s}^{-1}$ ) and the Mg II velocity dispersion w.r.t. [O III] ( $269 \text{ km s}^{-1}$ ) from Richards et al. (2002). These values are consistent with more recent determinations (Hewett & Wild 2010; Shen 2016; Shen et al. 2016).

(iii) If neither [O III] nor Mg II was usable, but broad H $\beta$  had been covered in our  $K$  band spectra, we took the H $\beta$  line, which reasonably traces the systemic frame. We adopted a blueshift of  $-109 \text{ km s}^{-1}$  and a velocity precision  $\sigma_v = 400 \text{ km s}^{-1}$  (Shen et al. 2016). Three quasars in our sample have H $\beta$  redshifts.

(iv) For the 10 quasars lacking near-infrared spectra of sufficient quality we measured the redshift from C IV covered in the optical spectra. We corrected for the known correlation of the C IV blueshift with continuum luminosity (Hewett & Wild 2010; Richards et al. 2011; Shen et al. 2016) using a sample of lower-redshift BOSS quasar spectra covering C IV and Mg II (see Paper I for details). Our determined blueshift w.r.t. Mg II

$$\Delta v = \left[ -192.4 - 599.6 \log \left( \frac{1450 \text{ \AA} \times L_{\lambda, 1450}}{10^{45} \text{ erg s}^{-1}} \right) \right] \text{ km s}^{-1} \quad (1)$$

is in reasonable agreement with the independent determination by Shen et al. (2016) for a distinct sample and line centring algorithm. Considering the large standard deviation  $\sigma_v = 656 \text{ km s}^{-1}$  of the corrected C IV redshifts w.r.t. the Mg II redshifts, we ignored the smaller spread of the Mg II redshifts about the systemic frame (Paper I).

For all five He II-transparent quasars with previous systemic redshift determinations (Mg II, H $\beta$ , H $\gamma$  and/or [O III]) from the literature our results are broadly consistent, in spite of differences in the employed methods (Table 2). The main sources of discrepancy are the treatment of line asymmetries and the averaging of results for multiple emission lines.

## 2.4 Absolute magnitudes and photon production rates

Optical photometry of the quasars was mainly obtained from SDSS Data Release 12 (Alam et al. 2015), with the exception of HE2QS J2311–1417 that has been covered in Data Release 1 of the Panoramic Survey Telescope and Rapid Response System 1 (Pan-STARRS1; Chambers et al. 2016; Flewelling et al. 2020), and HE 2347–4342 that has been taken from Worseck et al. (2008). For all quasars except HE 2347–4342 we determined the absolute

**Table 2.** He II-transparent quasars with measured systemic redshifts  $z_{\text{em}}$  from this work, which have previous redshift determinations  $z_{\text{other}}$  (Mg II, H $\beta$ , H $\gamma$ , [O III] or combinations thereof) from the literature.

Quasar	$z_{\text{em}}$	$z_{\text{other}}$	Reference
HS 1700+6416	$2.7472 \pm 0.0034$	$2.7510 \pm 0.0030$	Trainor & Steidel (2012)
HE 2347–4342	$2.8852 \pm 0.0006$	2.887	Syphers et al. (2011b)
		$2.886 \pm 0.001$	Shull & Danforth (2020)
Q 0302–003	$3.2850 \pm 0.0006$	$3.2860 \pm 0.0005$	Syphers & Shull (2014)
		$3.2859 \pm 0.0001$	Shen (2016)
		3.287	Zuo et al. (2015)
SDSS J1253+6817	$3.4753 \pm 0.0007$	3.2896	Coatman et al. (2017)
SDSS J2346–0016	$3.5076 \pm 0.0041$	3.4829	Coatman et al. (2017)
		$3.5110 \pm 0.0030$	Zheng et al. (2015)
		3.507	Zuo et al. (2015)

AB magnitude at rest-frame wavelength  $1450 \text{ \AA}$  from the extinction-corrected  $i$  band point-spread-function AB magnitude  $m_i$  as

$$M_{1450}(z_{\text{em}}) = m_i - 5 \log \left( \frac{d_L(z_{\text{em}})}{\text{Mpc}} \right) - 25 - K(z_{\text{em}}) \quad , \quad (2)$$

with the luminosity distance  $d_L$  in our adopted cosmology, and the bandpass correction  $K$  that was obtained by scaling the Lusso et al. (2015) quasar UV SED to the  $i$  band flux (Kulkarni et al. 2019). The latter assumption was necessary due to inaccurate relative fluxing of many of our HE2QS discovery spectra, and we estimate an error of 0.1 mag for  $M_{1450}$ . We used the Lusso et al. (2015) SED to estimate the quasar flux density at the H I Lyman limit  $f_{\nu, 912}$ . Assuming a power-law SED  $f_{\nu} \propto \nu^{-\alpha_{\nu}}$  at frequencies  $\nu > \nu_{912} = 3.2872 \times 10^{15} \text{ Hz}$ , the total He II-ionizing photon production rate is

$$Q = \frac{4\pi d_L^2}{(1+z_{\text{em}})} \int_{\nu_{228}}^{\infty} \frac{f_{\nu}}{h\nu} d\nu = \frac{4\pi d_L^2}{(1+z_{\text{em}})} \frac{4^{-\alpha_{\nu}} f_{\nu, 912}}{h\nu_{912}} \quad , \quad (3)$$

with Planck’s constant  $h\nu$  and the He II Lyman limit frequency  $\nu_{228} = 4\nu_{912}$ .

Due to cumulative IGM absorption by H I Lyman limit systems (e.g. Worseck & Prochaska 2011) and the He II Lyman series, the He II-ionizing power has to be inferred by extrapolation of the SED. As in Paper I we assumed a power-law SED slope  $\alpha_{\nu} = 1.5$  at  $\nu > \nu_{912}$ , consistent with recent measurements in stacked and composite quasar spectra (Shull et al. 2012; Stevans et al. 2014; Lusso et al. 2015). Since the actual value of  $\alpha_{\nu}$  depends on the chosen continuum windows, the total spectral coverage, and the exclusion of weak quasar emission lines (Stevans et al. 2014; Tilton et al. 2016), the large range in  $\alpha_{\nu}$  values from the literature is not surprising. SED reconstructions for two He II-transmitting quasars with complete spectral coverage indicate quasar-to-quasar variations in  $\alpha_{\nu}$  around our chosen value (Syphers & Shull 2013, 2014). A very hard SED ( $\alpha_{\nu} = 0.7$ ; Tilton et al. 2016) increases  $Q$  by a factor 6.5, but may violate constraints on the He II reionization history (Khaire 2017; Kulkarni et al. 2019). Very soft SEDs ( $\alpha_{\nu} \geq 2$ ; Lusso et al. 2018) are ruled out by the HST/COS spectra, and would lead to a modest  $\sim 0.4$  dex increase in the inferred quasar on-times (Paper I). Changes in the slope at  $\nu > \nu_{228}$  do not significantly change our results (Khrykin et al. 2016, 2019).

Equation (3) assumes that the escape fraction of He II-ionizing photons is unity. Recently, Shull & Danforth (2020) have suggested that many quasars could have escape fractions  $\approx 0.5$ – $0.9$  based on the observed range in the IGM He II/H I column density ratio. However, these observations are likely explained by radiative transfer in the IGM and the contribution of star-forming galaxies to the H I-ionizing background (e.g. Haardt & Madau 2012; Khaire & Srianand 2019; Puchwein et al. 2019; Faucher-Giguère 2020). In these models the required sample-averaged H I Lyman continuum escape fraction of galaxies is  $\sim 1$  per cent at  $z \sim 3$ , which is within recent observational

constraints (Grazian et al. 2017; Steidel et al. 2018; Fletcher et al. 2019). Therefore, the He II/H I column density ratio does not uniquely constrain the He II-ionizing escape fraction of unobscured quasars, such that our assumption of a unity escape fraction is justified.

## 2.5 Black hole masses and Eddington ratios

For the subset of 14 quasars with coverage of Mg II or H $\beta$  emission in their near-infrared spectra, single-epoch virial black hole masses were estimated from scaling relations

$$\log \left( \frac{M_{\text{BH}}}{M_{\odot}} \right) = a + b \log \left( \frac{\lambda_c L_{\lambda, \lambda_c}}{10^{44} \text{ erg s}^{-1}} \right) + 2 \log \left( \frac{\text{FWHM}}{\text{km s}^{-1}} \right), \quad (4)$$

with  $(\lambda_c, a, b) = (3000 \text{ \AA}, 0.86, 0.5)$  for Mg II (Vestergaard & Osmer 2009) and  $(\lambda_c, a, b) = (5100 \text{ \AA}, 0.91, 0.5)$  for H $\beta$  (Vestergaard & Peterson 2006).

Due to the varying spectral coverage and quality, measurements of the full width at half maximum (FWHM) of Mg (H $\beta$ ) were made for 10 (6) quasars. We adopt the H $\beta$  measurements when available. Table 3 lists the measurements and the derived quantities. The spectra were iteratively fit with a combination of a local power-law continuum, the Tsuzuki et al. (2006) Fe II emission template, and Gaussian emission line profiles. Due to the modest S/N, a single Gaussian was considered sufficient for most Mg II lines. Each H $\beta$  emission line was decomposed into one narrow and two broad Gaussians, and the nearby [O III] doublet was considered simultaneously with two Gaussians for each line of the doublet. Bayesian joint posterior distributions of the degenerate line parameters were estimated using the Goodman & Weare (2010) affine-invariant ensemble sampler for Markov Chain Monte Carlo (MCMC) as implemented in emcee (Foreman-Mackey et al. 2013). From the Mg II and H $\beta$  broad line parameter posterior distributions we computed the posterior probability density functions (PDFs) of the total FWHM, and adopt their median values and their equal-tailed 68 per cent credible intervals as our measurements and statistical uncertainties, respectively. Due to the inaccurate fluxing of the near-infrared spectra, the continuum luminosities at  $\lambda_c$  were estimated from  $M_{1450}$  by extrapolating the Lusso et al. (2015) power-law continuum  $f_{\nu} \propto \nu^{-0.61}$  obtained between 912 Å and 2500 Å, and assuming an uncertainty of 0.2 dex.

The propagated statistical uncertainties in  $M_{\text{BH}}$  are much smaller than the  $\approx 0.55$  dex uncertainty in the scaling relations, as estimated from the scatter of quasars with black hole masses from reverberation mapping (Vestergaard & Peterson 2006; Vestergaard & Osmer 2009; Shen 2013). Other scaling relations yield similar values to within 0.1–0.4 dex (McLure & Dunlop 2004; Ho & Kim 2015; Mejía-Restrepo et al. 2016; Woo et al. 2018; Bahk et al. 2019). We note that using the Tsuzuki et al. (2006) Fe II template instead of the Vestergaard & Wilkes (2001) template used to derive the Vestergaard & Osmer (2009) scaling relation may underestimate the black hole mass by  $\approx 0.2$  dex (Schindler et al. 2020). For the three quasars with Mg II and H $\beta$  FWHM measurements we obtained comparable virial black hole masses.

Bolometric luminosities were estimated with the bolometric correction at 1450 Å from Runnoe et al. (2012)

$$\log \left( \frac{L_{\text{bol}}}{\text{erg s}^{-1}} \right) = 4.74 + 0.91 \log \left( \frac{1450 \text{ \AA} \times L_{\lambda, 1450}}{\text{erg s}^{-1}} \right) - 0.12, \quad (5)$$

where the last term is their advocated correction of the biased viewing angle onto the quasar accretion disc. In a fully ionized primordial hydrogen and helium plasma the Eddington luminosity of a quasar

**Table 3.** Estimated black hole masses  $M_{\text{BH}}$  and Eddington ratios  $L_{\text{bol}}/L_{\text{Edd}}$  for the 14 quasars with measured total FWHM of Mg II or H $\beta$  decomposed into  $n_{\text{G}}$  Gaussian profiles. All quoted errors are  $1\sigma$  statistical uncertainties.

Quasar	Line	$n_{\text{G}}$	FWHM km s <sup>-1</sup>	$\log \left( \frac{M_{\text{BH}}}{M_{\odot}} \right)$	$\log \left( \frac{L_{\text{bol}}}{L_{\text{Edd}}} \right)$
HE 2347–4342	Mg II	2	4604 ± 19	9.44 ± 0.10	−0.54 ± 0.15
HS 1700+6416	Mg II	2	3837 ± 91	9.81 ± 0.10	0.05 ± 0.15
HS 1024+1849	Mg II	1	5690 ± 415	9.79 ± 0.12	−0.59 ± 0.16
Q 1602+576	Mg II	1	2285 ± 91	9.09 ± 0.11	0.28 ± 0.15
PC 0058+0215	Mg II	1	3930 ± 320	9.26 ± 0.12	−0.44 ± 0.16
SDSS J0936+2927	Mg II	1	2650 ± 92	9.06 ± 0.10	0.02 ± 0.15
SDSS J1237+0126	Mg II	1	2192 ± 274	8.79 ± 0.15	0.10 ± 0.18
SDSS J2346–0016	Mg II	1	3474 ± 137	9.45 ± 0.11	−0.09 ± 0.15
Q 0302–003	H $\beta$	2	3017 ± 320	9.38 ± 0.14	0.07 ± 0.17
HE2QS J2157+2330	H $\beta$	2	3659 ± 324	9.46 ± 0.13	−0.17 ± 0.17
HS 0911+4809	H $\beta$	2	2872 ± 1002	9.27 ± 0.32	0.05 ± 0.34
SDSS J1253+6817	H $\beta$	2	4845 ± 1006	9.59 ± 0.21	−0.51 ± 0.23
HE2QS J1630+0435	H $\beta$	2	4128 ± 230	9.69 ± 0.11	−0.18 ± 0.16
SDSS J1319+5202	H $\beta$	2	5403 ± 867	9.85 ± 0.17	−0.47 ± 0.20

is (Shapiro 2005; Madau et al. 2014)<sup>5</sup>

$$L_{\text{Edd}} = \frac{4\pi G c m_p}{\sigma_{\text{T}}(1 - Y/2)} M_{\text{BH}} = 1.43 \times 10^{38} \left( \frac{M_{\text{BH}}}{M_{\odot}} \right) \text{ erg s}^{-1}, \quad (6)$$

where  $m_p$  is the proton mass,  $\sigma_{\text{T}}$  is the Thomson scattering cross section, and natural constants are written in their usual symbols. Expressing Equation (5) in magnitudes, the logarithmic Eddington ratio is

$$\log \left( \frac{L_{\text{bol}}}{L_{\text{Edd}}} \right) = -0.364 M_{1450} - \log \left( \frac{M_{\text{BH}}}{M_{\odot}} \right) - 0.82. \quad (7)$$

Again, the statistical uncertainties in the Eddington ratios listed in Table 3 are smaller than the  $\approx 0.55$  dex systematic uncertainty induced by the virial black hole mass scaling relations.

## 3 MEASURED HE II PROXIMITY ZONE SIZES

In the quasar proximity zone the gas is more highly ionized, visible in the spectrum as excess Ly $\alpha$  transmission. One wishes to robustly quantify its extent while limiting the impact of small-scale density fluctuations and observational effects in heterogeneous samples, such as differences in spectral resolution and S/N. To that aim, we adopted a procedure similar to work on H I quasar proximity zones at  $z_{\text{em}} \sim 6$  (e.g. Fan et al. 2006; Carilli et al. 2010; Eilers et al. 2017), and smoothed the normalized *HST*/COS spectra with a Gaussian filter with an FWHM of 1 pMpc at the respective quasar redshift. The smoothing FWHM corresponds to 4.5–8.5 pixels in our COS G140L spectra binned to 0.24 Å pixel<sup>-1</sup>. The proximity zone size  $R_{\text{pz}}$  is then defined as the cosmological proper distance to the first pixel where the smoothed normalized flux drops below 0.1. At  $z > 3$  the intergalactic He II Ly $\alpha$  transmission on similar scales rarely exceeds this threshold (Worseck et al. 2016, 2019), such that the He II proximity zones are well defined. At lower redshifts the He II proximity zone sizes become less distinct due to the emerging post-reionization He II Ly $\alpha$  forest. However, our radiative transfer simulations (Section 4.1) account for density fluctuations in a predominantly ionized IGM with an initial He II fraction as low as 1 per cent, consistent with the inferences from the He II Ly $\alpha$  forest (Worseck et al. 2019). Furthermore, we verified with realistic mock spectra that our *HST*/COS spectra are of sufficient quality to yield robust proximity zone sizes (Appendix A). Consequently, our quoted uncertainties  $\sigma_{R_{\text{pz}}}$  on the

<sup>5</sup> We note that in the literature, most expressions for the quasar Eddington luminosity incorrectly assume a pure hydrogen plasma.

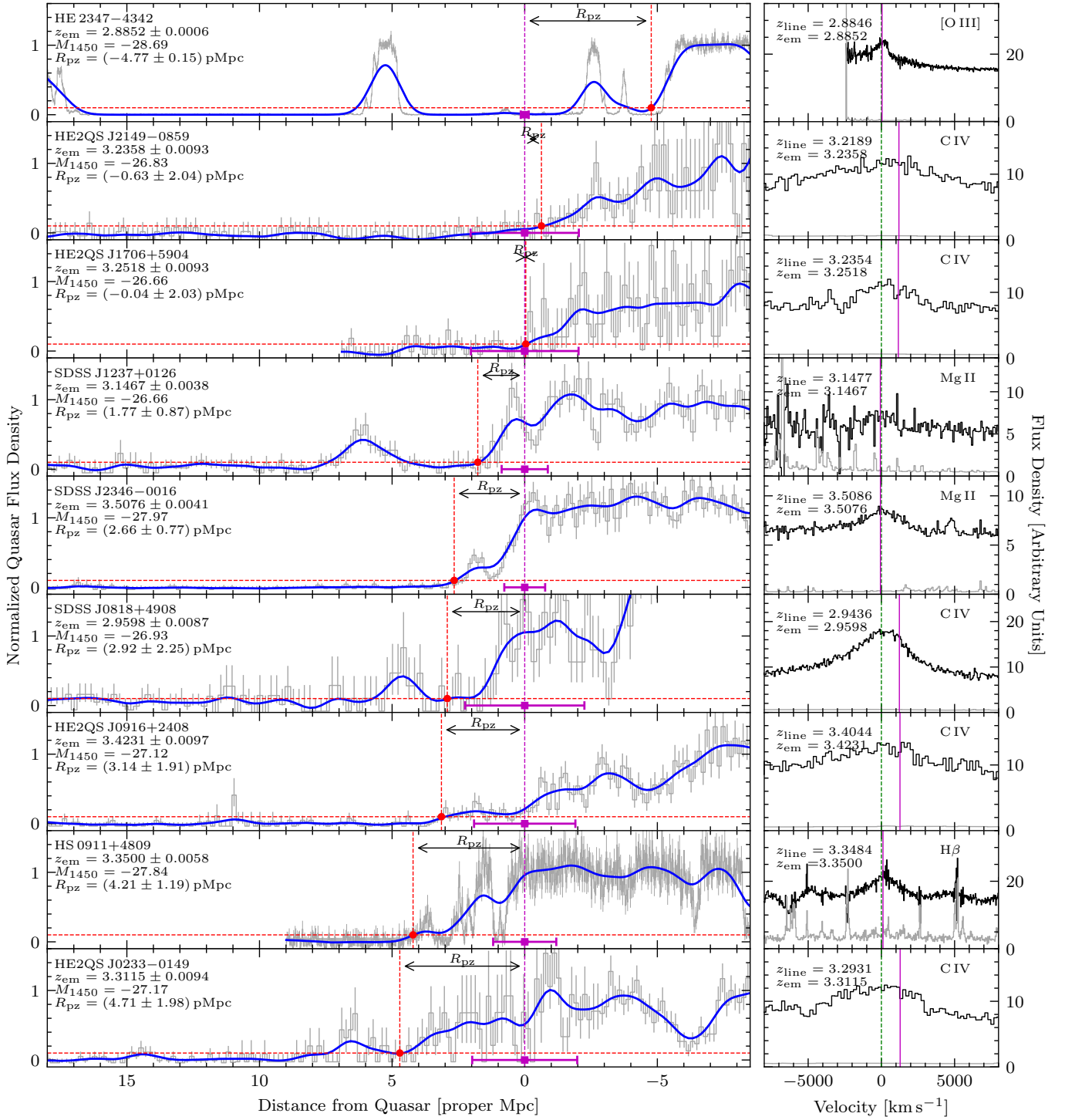


**Figure 1.** *Left:* Normalized *HST/COS* spectra (grey; overplotted error bars are statistical  $1\sigma$  Poisson errors) of nine  $z_{em} < 3.6$  quasars from Table 1 with measured small He II proximity zone sizes  $R_{pz} < 5$  pMpc (labelled). Distances are for the He II Ly $\alpha$  transition relative to the quasar at the estimated systemic redshift  $z_{em}$ . With this sign convention, absorption at distances  $\ll 0$  is due to infalling He II gas clouds or foreground H I, while absorption at large distances is dominated by intergalactic He II. The violet squares with error bars mark the quasar redshift uncertainties. The blue lines show the normalized flux smoothed with a Gaussian filter with FWHM = 1 pMpc. The red dots mark the measured  $R_{pz}$ , defined as the position where the smoothed flux falls below 0.1. *Right:* Spectral regions of the labelled quasar emission lines used to estimate the systemic redshifts. The flux density is shown in black, whereas the grey lines show the corresponding  $1\sigma$  error array. Vertical dashed lines mark the measured mode of the emission lines, yielding the emission line redshifts  $z_{line}$ . The vertical solid lines mark the applied velocity offsets to estimate the systemic redshifts  $z_{em}$ .



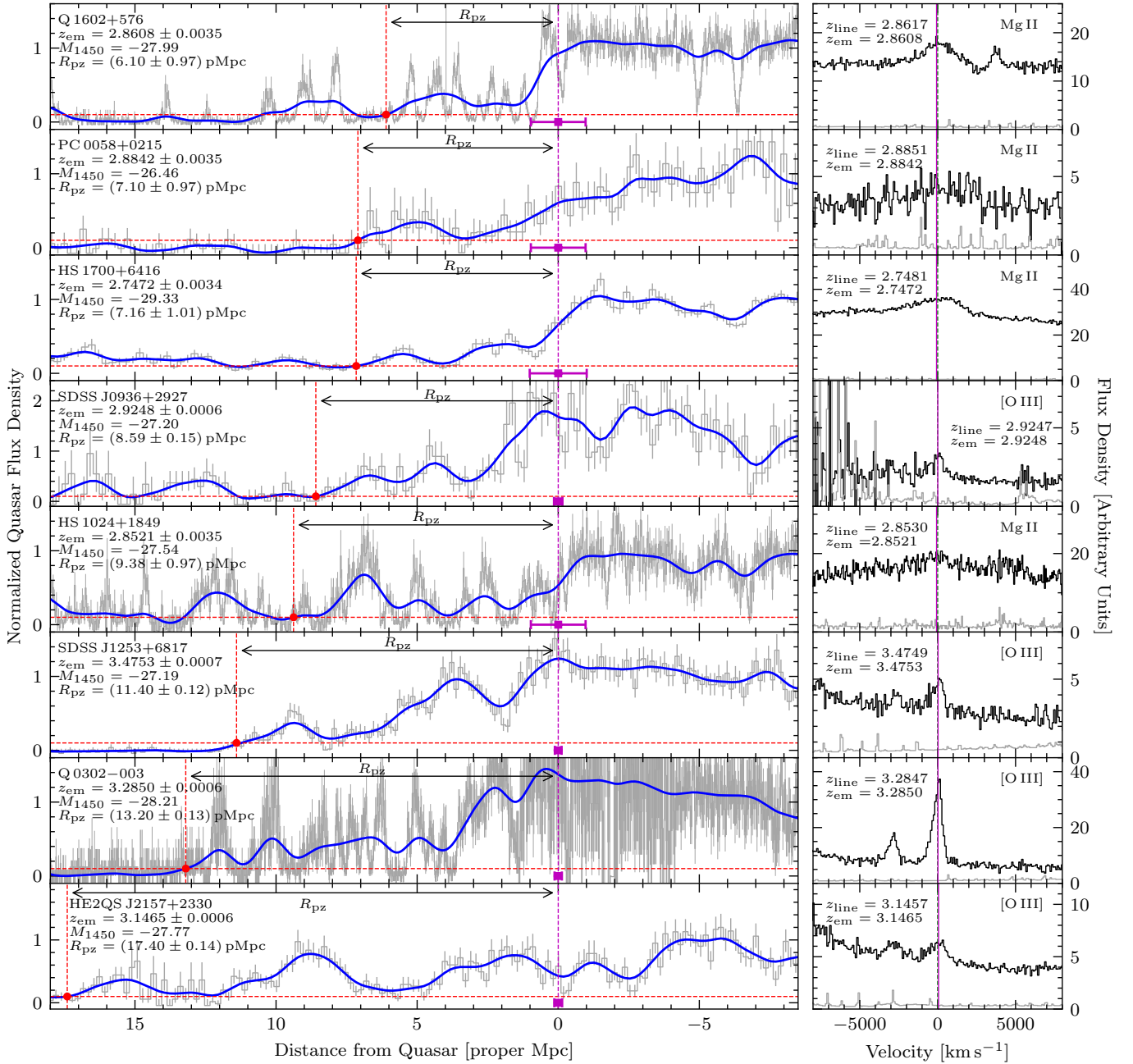


**Figure 2.** Similar to Fig. 1 for eight  $z_{em} < 3.6$  quasars with large He II proximity zone sizes  $R_{pz} > 5$  pMpc.

proximity zone sizes are based on the individual quasar redshift uncertainties, ranging from  $\sim 0.1$  pMpc ([O III]) to  $\approx 2$  pMpc (C IV).

Figures 1 and 2 show the He II proximity zone spectra of the 17  $z_{em} < 3.6$  quasars from Table 1, ordered by their measured  $R_{pz}$ . We also show the spectral regions of the UV-optical emission lines used to determine their systemic redshifts. The smoothed normalized flux drops significantly within several proper Mpc of each quasar, which a posteriori justifies our chosen smoothing scale. The flux shows some contamination from unrelated low-redshift absorption (e.g. at negative distances in Fig. 1 and 2), but this contamination is very unlikely to affect the measurements of He II proximity zone sizes. We see strong diversity in the proximity zone sizes and flux profiles. Most He II proximity zones show structure due to IGM

density fluctuations and radiative transfer effects, both of which have been probed with high-resolution optical spectra of the coeval H I Ly $\alpha$  absorption (Reimers et al. 1997; Hogan et al. 1997; Anderson et al. 1999; Heap et al. 2000; Smette et al. 2002; Fechner & Reimers 2007; Shull et al. 2010; Syphers & Shull 2013, 2014; Zheng et al. 2019).

The accurate and precise redshifts of all quasars plotted in Fig. 2 suggest that large He II proximity zone sizes  $R_{pz} > 5$  pMpc are common. Even with less precise redshifts their proximity zones would be much larger than the ones shown in Fig. 1. Measurements of small He II proximity zones are often hampered by the large C IV quasar redshift uncertainty, limiting the further use of ten quasars from our combined sample (Table 1). The five  $z_{em} < 3.6$  quasars with C IV red-



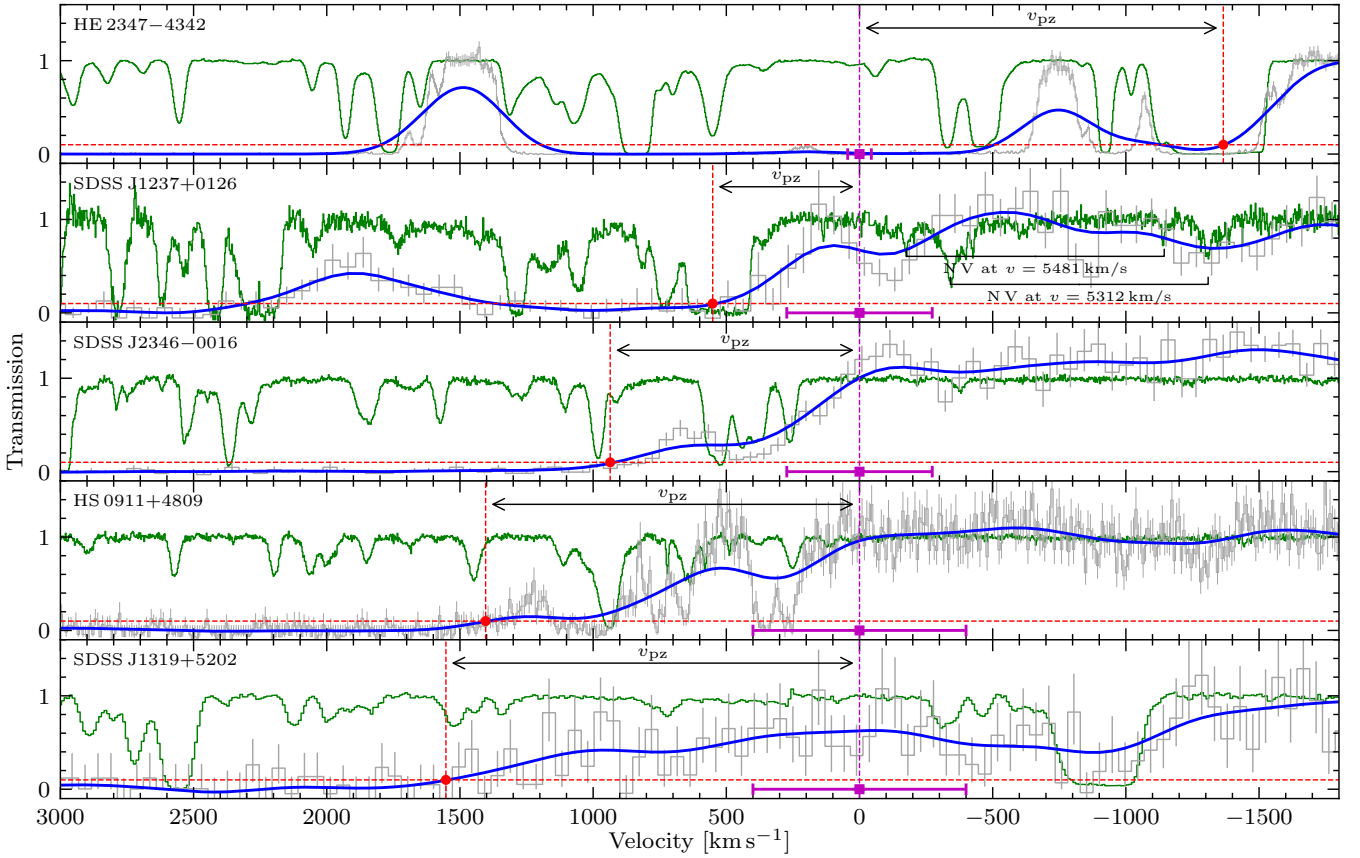


**Figure 3.** Normalized *HST*/COS UV spectra (grey) and optical spectra (green) of the five quasars with sufficiently precise redshifts ( $\sigma_v \leq 400 \text{ km s}^{-1}$ ; violet square with error bar) to measure small He II proximity zones ( $R_{\text{pz}} < 5 \text{ pMpc}$ ). Velocities are for He II and H I with respect to the quasar, with  $v < 0$  indicating infalling gas. As in Fig. 1 we also show the smoothed normalized UV flux (blue) with the corresponding velocity width  $v_{\text{pz}}$  of the He II proximity zone. Note the different resolving powers for the H I spectra (SDSS J1319+5202:  $R \sim 5400$ ;  $R \sim 45,000$  otherwise) and the He II spectra (HE 2347–4342:  $R \approx 17,000$ ; HS 0911+4809:  $R \approx 10,000$ ;  $R \approx 2400\text{--}2700$  otherwise).

shifts are marked in Fig. 1. The significant absorption at negative distances in the spectra of HE2QS J2149–0859, HE2QS J1706+5904, and HE2QS J0916+2408 in Fig. 1 suggests very large blueshifts of C IV relative to systemic, similar to HE2QS J2354–2033 from Paper I. In Fig. 3 we show the He II and the corresponding H I spectra of the five quasars that have sufficiently precise redshifts to measure small He II proximity zone sizes  $R_{\text{pz}} < 5 \text{ pMpc}$  ( $\sigma_v \leq 400 \text{ km s}^{-1}$  corresponding to  $\sigma_{R_{\text{pz}}} < 1.2 \text{ pMpc}$ ). Coincident absorption in H I and He II identifies gas flows in the quasar environment. Large infall velocities  $v \lesssim -1000 \text{ km s}^{-1}$  may not be correctly captured by our simulations, hampering estimates of the quasar on-time.

The luminous quasar HE 2347–4342 lacks a He II proximity zone, which is likely explained by its peculiar associated absorption system (Reimers et al. 1997; Fechner et al. 2004). Many of its N V and O VI bearing components are consistent with being photoionized by the quasar (Fechner et al. 2004). Because their He II column densities are insufficient to shield He II-ionizing photons, Shull et al. (2010) argued that HE 2347–4342 has recently turned on ( $t_{\text{on}} < 1 \text{ Myr}$ ). However, the location of the absorbing gas is unconstrained. The accurate and precise [O III] redshift  $z_{\text{em}} = 2.8852 \pm 0.0006$  implies large gas infall velocities of  $\sim 1500 \text{ km s}^{-1}$  onto the circumnuclear region (Fig. 3), and even higher velocities if the gas resides in the circumgalactic medium of the host galaxy. Redshift space distortions (Hui et al. 1997; Weinberg et al. 1997) significantly affect the He II transmission profile, possibly masking the He II proximity ef-

fect altogether. Conclusive evidence for or against HE 2347–4342 being a young quasar requires detailed numerical modelling of gas associated with the quasar or its host galaxy, which is outside the scope of this work. Because of the extreme peculiar gas velocities that are not represented in our simulations (Section 4.1), we exclude HE 2347–4342 from further discussion.

The other four quasars shown in Fig. 3 are less extreme. SDSS J1237+0126 has a blended optically thin H I system at  $v \approx 500 \text{ km s}^{-1}$  that is likely responsible for its small measured He II proximity zone. No high-velocity infall is detected. The He II transmission at  $1500\text{--}2200 \text{ km s}^{-1}$  may belong to the proximity zone. However, provided that our simulations approximately capture the density and velocity field around the quasar host halo, our strict and simple definition of  $R_{\text{pz}}$  ensures a one-to-one comparison to our models (Section 4.1) that include cases of misestimated proximity zone sizes due to the density field and peculiar velocities, similar to recent work on  $z_{\text{em}} \sim 6$  H I proximity zones (Eilers et al. 2017, 2020). The strong N V absorbers at 5312 and 5481  $\text{km s}^{-1}$  may either indicate a much larger proximity zone of SDSS J1237+0126 or a high-velocity outflow. The He II spectra of SDSS J2346–0016 and HS 0911+4809 are modulated by the density field and H I absorption. Their short He II proximity zones do not seem affected by peculiar velocities. Finally, SDSS J1319+5202 from Paper I shows a possibly infalling H I complex at  $v \approx -900 \text{ km s}^{-1}$  with strong associated C IV and N V in two components. The complex does not affect

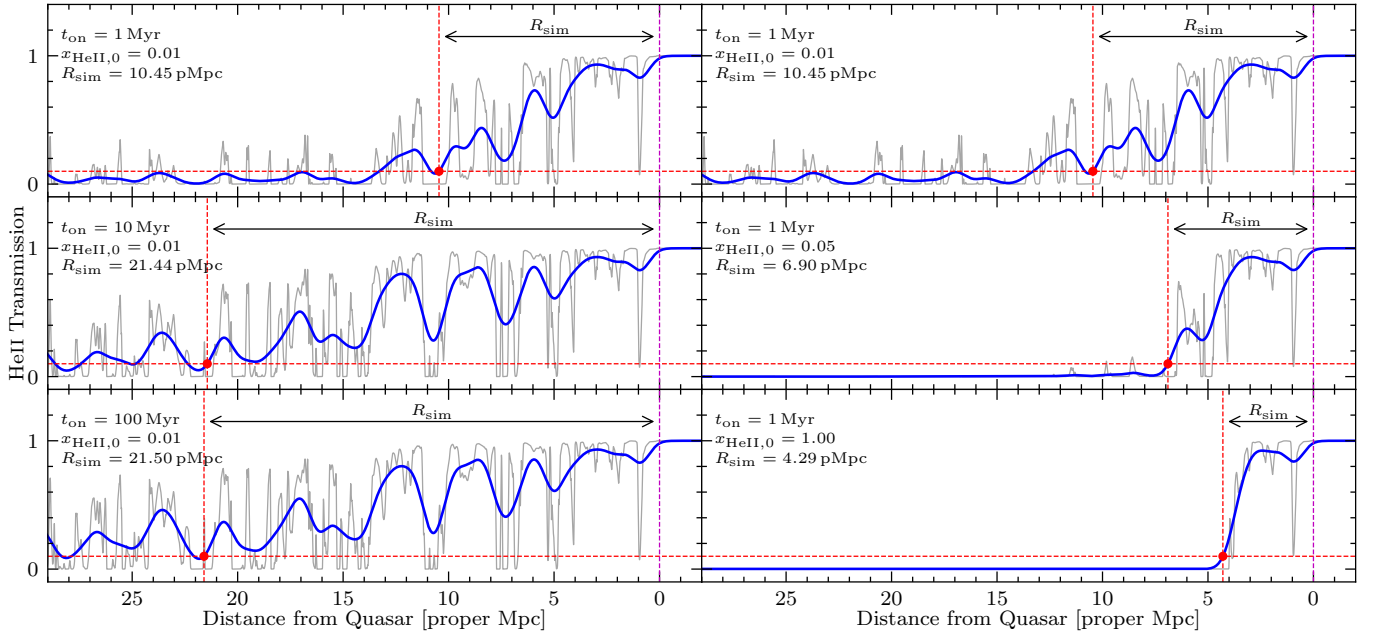


**Figure 4.** Examples of He II transmission spectra from our one-dimensional radiative transfer models of Q 1602+576 ( $z_{\text{em}} = 2.8608$ ,  $M_{1450} = -27.99$ ,  $Q = 10^{56.80} \text{ s}^{-1}$ ). Resolved (smoothed) spectra are shown in grey (blue). The red dots mark the proximity zone sizes  $R_{\text{sim}}$  measured from the smoothed spectra. The left panels show the increase of  $R_{\text{sim}}$  with the quasar on-time  $t_{\text{on}}$  for a fixed initial He II fraction  $x_{\text{HeII},0} = 0.01$ , whereas the right panels show the decrease of  $R_{\text{sim}}$  with increasing  $x_{\text{HeII},0}$  for a fixed quasar on-time  $t_{\text{on}} = 1 \text{ Myr}$ .

the measurement of  $R_{\text{pz}}$  because the H I absorption in the rest of the proximity zone is much lower than expected for the  $z \approx 3.9$  H I Ly $\alpha$  forest. In summary, except for the peculiar quasar HE 2347–4342, gas inflows and outflows seen in absorption do not substantially affect our measurements of small He II proximity zone sizes. Excluding HE 2347–4342 and HE2QS J2354–2033 from Paper I that has an anomalously large C IV blueshift, 22 quasars remain in our sample. Thirteen of them have sufficiently precise systemic redshifts ( $\sigma_v \leq 400 \text{ km s}^{-1}$ ) and black hole masses from near-infrared spectra.

## 4 THEORETICAL METHODS

### 4.1 Radiative transfer models of He II proximity zones

To explain the diversity in the measured proximity zone sizes and to infer the on-times of the quasars, we used a combination of hydrodynamical simulations and one-dimensional radiative transfer simulations of He II quasar proximity zones, described in detail in Khrykin et al. (2016, 2017). For their cosmological setting, we used the output of a Gadget-3 (Springel 2005) smooth particle hydrodynamics simulation run in a cubic volume of  $(25h^{-1})^3$  comoving  $\text{Mpc}^3$  containing  $512^3$  baryonic and dark matter particles, respectively. Using periodic boundary conditions, we drew 1000 one-dimensional density, velocity, and temperature distributions (skewers) in random directions around the most massive halo in the  $z_{\text{sim}} = 3.1$  snapshot of the simulation. Assuming that cosmic structure evolution is negligible between  $z_{\text{sim}}$  and the quasar redshifts (Table 1), we accounted for density evolution by rescaling the gas densities by a factor  $(1+z_{\text{em}})^3/(1+z_{\text{sim}})^3$ . The resulting skewers have a length of 160 comoving Mpc, sampled at  $dr = 11.9$  comoving kpc, corresponding to  $dv = 0.86\text{--}0.93 \text{ km s}^{-1}$  at  $z_{\text{em}} = 2.74\text{--}3.5$ .

The skewers were processed with a one-dimensional radiative transfer algorithm based on the C<sup>2</sup>-Ray code (Mellema et al. 2006),

which tracks the evolution of H I, He II,  $e^-$ , and the gas temperature to generate He II Ly $\alpha$  transmission spectra of quasar proximity zones (Khrykin et al. 2016, 2017). Analogous to Paper I, we created a set of radiative transfer models for each quasar at its respective redshift  $z_{\text{em}}$  and photon production rate  $Q$  (Table 1), varying the quasar on-time  $t_{\text{on}}$  and the initial He II fraction in the ambient IGM at quasar turn-on  $x_{\text{HeII},0}$  (or equivalently the UV background photoionization rate  $\Gamma_{\text{HeII}}$ ). We assumed for simplicity that the quasars emitted continuously at their inferred luminosity for a time  $t_{\text{on}}$  prior to our observation, i.e. as a “light bulb”. We considered a base-10 logarithmically spaced grid of on-times  $\log(t_{\text{on}}/\text{Myr}) \in [-2, 2]$  with a step size  $\Delta \log(t_{\text{on}}/\text{Myr}) = 0.125$ . For the initial He II fraction we took the inhomogeneously spaced grid  $x_{\text{HeII},0} \in \{0.01, 0.05, 0.1, 0.2, 0.3, 0.5, 0.6, 0.7, 0.9, 1.0\}$ . Because the quasars are at lower redshifts than those from Paper I we included models with  $x_{\text{HeII},0} = 0.01$  representative of the IGM at the end of He II reionization (Khrykin et al. 2016; Worseck et al. 2019). This resulted in a grid of 330 radiative transfer models per quasar, each with 1000 He II Ly $\alpha$  transmission spectra. Redshift error is incorporated in our Bayesian inference (Section 4.2).

Figure 4 shows an example of model He II proximity zone spectra varying  $t_{\text{on}}$  (left) and  $x_{\text{HeII},0}$  (right) for the same density skewer. The model proximity zone size  $R_{\text{sim}}$  measured analogously to the HST/COS spectra (Section 3) depends on the quasar on-time, as the IGM responds to changes in the radiation field on the He II equilibration time-scale  $t_{\text{eq}} \approx \Gamma_{\text{HeII}}^{-1} \approx 30 \text{ Myr}$  in the  $z \sim 3$  IGM (Khrykin et al. 2016). For  $t_{\text{on}} \lesssim t_{\text{eq}}$  the proximity zone size increases with  $t_{\text{on}}$ , but stalls for longer on-times (Paper I), as illustrated in the lower left panel of Fig. 4. The proximity zone size only weakly depends on the initial IGM He II fraction due to the thermal proximity effect (Khrykin et al. 2017) and the definition of the proximity zone size that does not probe the actual size of the ionized region (Khrykin et al. 2016). Only at the lowest initial He II fractions  $x_{\text{HeII},0} < 0.05$ ,

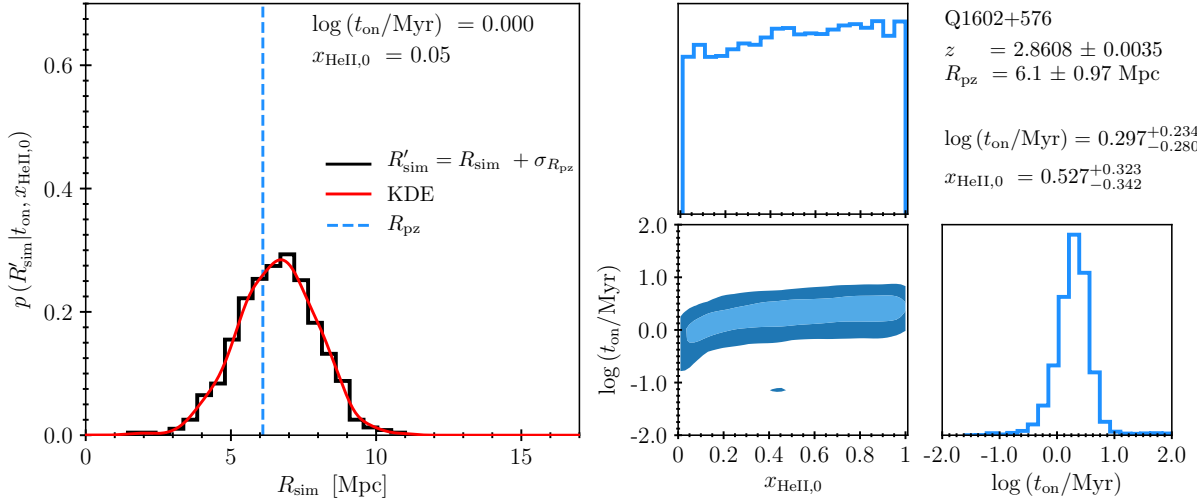


**Figure 5.** Example of our Bayesian inference of the quasar on-time for Q 1602+576. Left: PDF of the modelled He II proximity zone size including measurement error as a kernel density estimate (red) of the 1000 realizations (black) for an on-time  $t_{\text{on}} = 1$  Myr and an initial He II fraction  $x_{\text{He II},0} = 0.05$ . The dashed line marks the measured He II proximity zone size. Right: Constraints on the quasar on-time and the initial He II fraction from the Bayesian inference. The 95 per cent (dark blue) and 68 per cent (light blue) credible regions from the MCMC calculations are shown. The histograms illustrate the corresponding estimated marginalized posterior PDFs.

$R_{\text{sim}}$  falls at sufficiently large distances where the quasar does not dominate the total He II photoionization rate (Fig. 4), such that the proximity zone size becomes weakly sensitive to  $x_{\text{He II},0}$ . This weak sensitivity combined with quasar redshift uncertainties makes it challenging to infer  $x_{\text{He II},0}$  (Paper I). Furthermore, the joint distribution  $R_{\text{sim}}(t_{\text{on}}, x_{\text{He II},0})$ , estimated from the 1000 spectra per model, is significantly blurred by density fluctuations at low initial He II fractions. We did not account for the lower resolving power of our *HST*/COS spectra or their data quality, because they do not significantly affect our results (Appendix A).

## 4.2 Bayesian inference of the quasar on-time

To estimate the on-times of individual quasars in our sample, we performed MCMC inference on their measured He II proximity zones  $R_{\text{pz}}$  using the Bayesian statistical method introduced in Paper I. First, we incorporated the individual quasar redshift uncertainties into the radiative transfer models by adding a Gaussian-distributed random deviate with a standard deviation  $\sigma_{R_{\text{pz}}}$  (Table 1) to each  $R_{\text{sim}}$  realization, similar to Paper I. For each resulting distribution  $R'_{\text{sim}}$  we can write a Bayesian likelihood  $\mathcal{L}$  given the combination of model parameters  $\{t_{\text{on}}, x_{\text{He II},0}\}$  per quasar,

$$\mathcal{L}(R_{\text{pz}}|t_{\text{on}}, x_{\text{He II},0}) = p(R'_{\text{sim}} = R_{\text{pz}}|t_{\text{on}}, x_{\text{He II},0}) \quad (8)$$

where  $p(R'_{\text{sim}} = R_{\text{pz}}|t_{\text{on}}, x_{\text{He II},0})$  is the PDF of the modelled He II proximity zone sizes plus redshift error  $R'_{\text{sim}}$ , evaluated at the value of the measured He II proximity zone size  $R_{\text{pz}}$ . To construct this PDF we used kernel density estimation (KDE) on the respective set of 1000 model spectra. An example KDE on the distribution of proximity zone sizes in one radiative transfer model is illustrated in the left panel of Fig. 5. We then computed the likelihood of each radiative transfer model in our  $\{t_{\text{on}}, x_{\text{He II},0}\}$  grid via Equation (8), and constructed each quasar's continuous two-dimensional likelihood by bivariate spline interpolation.

To infer  $t_{\text{on}}$  for each individual quasar we sampled the respective likelihood with MCMC. Because the initial He II fraction is quite

uncertain at the redshifts of interest due to large-scale UV background fluctuations at the tail end of He II reionization (Davies et al. 2017; Worseck et al. 2019), we chose to impose a uniform prior  $0.01 \leq x_{\text{He II},0} \leq 1$ . Similarly, we set a uniform prior on  $\log(t_{\text{on}}/\text{Myr})$  in the range  $0.01\text{--}100$  Myr. The lower limit is motivated by the ubiquitous H I proximity effect implying  $t_{\text{on}} \gtrsim \Gamma_{\text{H I}}^{-1} \approx 0.03$  Myr at  $z \sim 3$  except for the few youngest  $z_{\text{em}} \gtrsim 6$  quasars in Eilers et al. (2020). The upper limit of 100 Myr is driven by estimates of the quasar duty cycle ( $t_{\text{dc}} = 1\text{--}1000$  Myr, e.g. Yu & Tremaine 2002; White et al. 2008). Furthermore, approximations of our modelling break down at longer on-times for two reasons: i)  $t_{\text{on}}$  becomes comparable to the cooling time meaning that cooling cannot be neglected; ii) our assumption of a static density field for the radiative transfer in post-processing is not valid anymore (Khrykin et al. 2016).

As an example, we show the results of the MCMC inference for the quasar Q 1602+576 in the right panels of Fig. 5. Analogous to the results in Paper I, the flat posterior PDF of  $x_{\text{He II},0}$  signals the lack of sensitivity of the He II proximity zone size to the initial He II fraction in the IGM. Yet, we are able to put tight constraints on the on-time of Q 1602+576 due to the small uncertainty in its proximity zone size facilitated by its accurate and precise systemic redshift (Table 1).

## 5 RESULTS

### 5.1 He II proximity zone sizes do not scale with luminosity or redshift

Many studies on  $z_{\text{em}} \sim 6$  H I quasar proximity zones (Maselli et al. 2007, 2009; Bolton & Haehnelt 2007; Lidz et al. 2007; Keating et al. 2015; Eilers et al. 2017; Davies et al. 2020) and on  $z_{\text{em}} \sim 4$  He II proximity zones (Khrykin et al. 2016, 2019) have emphasized that by definition  $R_{\text{pz}}$  probes fully reionized gas in the quasar vicinity, and is always smaller than the actual size of the ionized region. Moreover, simple scaling laws with luminosity  $R \propto 10^{-0.4\gamma M_{1450}}$  with  $\gamma = 1/3$  ( $\gamma = 1/2$  for a neutral (ionized) IGM) do not apply for smoothed spectra and a realistic IGM density field (Bolton & Haehnelt 2007;

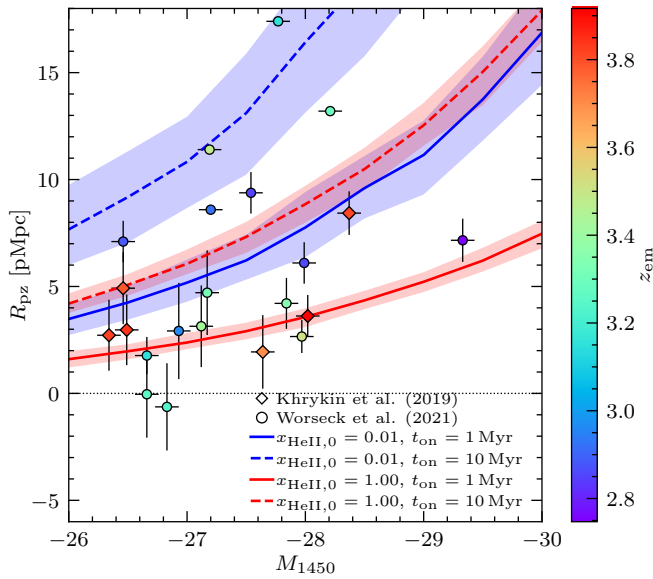


**Figure 6.** He II proximity zone size  $R_{\text{pz}}$  as a function of quasar absolute magnitude  $M_{1450}$  for the 22 quasars in our combined sample. Circles and diamonds mark  $z_{\text{em}} < 3.6$  and higher-redshift quasars (Paper I), respectively. The colour coding indicates the quasar redshift.  $R_{\text{pz}}$  errors have been calculated from the individual redshift errors. The dotted line marks  $R_{\text{pz}} = 0$ . Overplotted is the average  $R_{\text{pz}}(M_{1450})$  and its 16–84th percentile scatter from our radiative transfer simulations at  $z_{\text{em}} = 3.29$  for different initial He II fractions  $x_{\text{HeII},0}$  and quasar on-times  $t_{\text{on}}$ .

Davies et al. 2020). Although the H I proximity zone sizes of  $z_{\text{em}} \sim 6$  quasars generally increase with luminosity (Eilers et al. 2017), 5–10 per cent of the population has undersized proximity zones that likely indicate short on-times  $t_{\text{on}} \lesssim 0.01\text{--}0.1$  Myr (Eilers et al. 2018, 2020).

Figure 6 shows the measured He II proximity zone size  $R_{\text{pz}}$  as a function of absolute magnitude  $M_{1450}$  for the combined sample of 22 quasars, i.e. Table 1 excluding HE 2347–4342 and HE2QS J2354–2033. We see no clear relation between  $R_{\text{pz}}$  and  $M_{1450}$ . For the eight  $M_{1450} \sim -28$  quasars with precise systemic redshifts there is a factor  $\sim 5$  spread in  $R_{\text{pz}}$ . We overplot predictions of the average  $R_{\text{pz}}(M_{1450})$  from our radiative transfer simulations at the median redshift  $z_{\text{em}} = 3.29$  of our combined sample<sup>6</sup>. The model predictions for extreme values of the IGM He II fraction before quasar turn-on  $x_{\text{HeII},0} \in \{0.01, 1\}$  and two representative on-times  $t_{\text{on}} \in \{1 \text{ Myr}, 10 \text{ Myr}\}$  cover a similar range of  $R_{\text{pz}}$  as the observations. IGM density fluctuations give rise to intrinsic scatter in the simulated  $R_{\text{pz}}$  that increases toward low He II fractions, i.e. in the emerging He II Ly $\alpha$  forest. The He II fraction and the on-time are often degenerate (Khrykin et al. 2016, 2019), as illustrated by the overlapping curves for  $(x_{\text{HeII},0}, t_{\text{on}}) = (0.01, 1 \text{ Myr})$  and  $(x_{\text{HeII},0}, t_{\text{on}}) = (1, 10 \text{ Myr})$ . Nevertheless, the smallest precisely measured He II proximity zone sizes require short on-times of  $\lesssim 1$  Myr, whereas the largest ones require long on-times of  $\gtrsim 10$  Myr. Therefore, our measurements are sensitive to  $t_{\text{on}}$  up to the He II equilibration time-scale  $t_{\text{eq}} \approx 30 \text{ Myr}$  at  $z \sim 3$  (Khrykin et al. 2016, 2019).

Our finding that He II proximity zone sizes do not scale with luminosity unlike their  $z_{\text{em}} \sim 6$  H I counterparts, can be explained by

<sup>6</sup> We verified that these relations do not change dramatically due to IGM density evolution in the redshift range of interest.

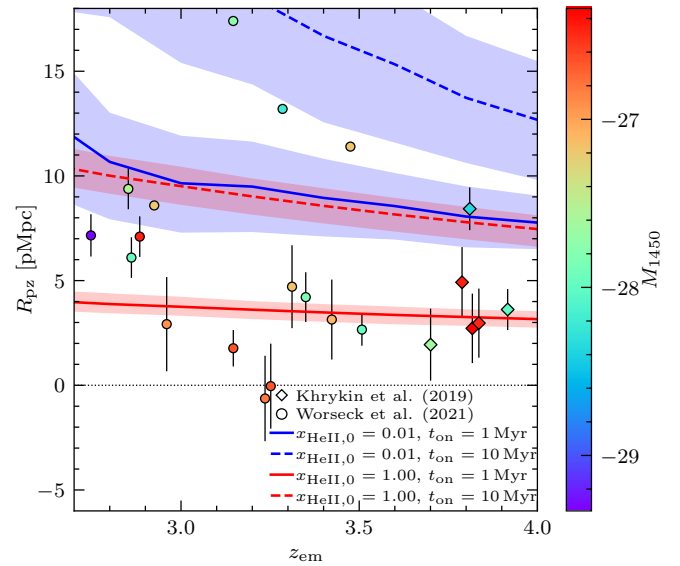


**Figure 7.** Similar to Fig. 6 for the He II proximity zone size  $R_{\text{pz}}$  as a function of quasar redshift  $z_{\text{em}}$ . The colour coding indicates the quasar absolute magnitude. Overplotted is the average  $R_{\text{pz}}(z_{\text{em}})$  and its 16–84th percentile scatter from our radiative transfer simulations at  $M_{1450} = -27$  for different initial He II fractions  $x_{\text{HeII},0}$  and quasar on-times  $t_{\text{on}}$ .

the lack of sensitivity of H I proximity zone sizes to  $t_{\text{on}} \gtrsim 0.1$  Myr, which is rooted in the shorter H I equilibration time-scale. If most  $z_{\text{em}} \sim 6$  quasars shone longer than 0.1 Myr, their similar H I proximity zone sizes result in an overall strong scaling with luminosity (Davies et al. 2020), with shorter on-times being apparent as outliers (Eilers et al. 2017, 2018, 2020). In contrast, He II proximity zone sizes probe  $t_{\text{on}} \lesssim 30 \text{ Myr}$ , so variations in the individual on-times can effectively remove any correlation with luminosity.

As shown in Fig. 7 the He II proximity zone size does not depend on redshift. Some of the scatter in  $R_{\text{pz}}$  vs. redshift is due to the  $\approx 3$  mag range in  $M_{1450}$ , but due to the lack of a clear correlation with luminosity we do not take out this dependence. The large scatter in  $R_{\text{pz}}$  for the eight quasars at  $M_{1450} \sim -28$  with precise systemic redshifts confirms that there is no evidence for a scaling with redshift. Our measurements do not support previous claims of a significant decline of the luminosity-normalized  $R_{\text{pz}}$  at  $z_{\text{em}} > 3.3$  by Zheng et al. (2015) for a slightly different definition of the proximity zone size that does not track the quasar ionization front (Khrykin et al. 2016). At fixed luminosity our radiative transfer simulations show a shallow decrease of  $R_{\text{pz}}$  with redshift for a large range of on-times and IGM He II fractions (Fig. 7). This is a direct consequence of the observational definition of  $R_{\text{pz}}$  and its insensitivity to the IGM He II fraction (Khrykin et al. 2016, 2019). Only for long on-times and small He II fractions is there a significant decrease with redshift that is driven by IGM density evolution. Similar shallow relations have been obtained for H I proximity zones at  $z_{\text{em}} \sim 6$  (Eilers et al. 2017; Davies et al. 2020). For the model relations in Fig. 7 we chose  $M_{1450} = -27$ , somewhat fainter than the median  $M_{1450}$  of our sample, in order to facilitate comparison with Eilers et al. (2017). For the three  $M_{1450} \sim -27$  quasars from Paper I small but uncertain proximity zone sizes indicate  $t_{\text{on}} \ll 10 \text{ Myr}$  irrespective of the initial IGM He II fraction, consistent with our joint analysis in Paper I. On the other hand, the large He II proximity zone of the  $M_{1450} \sim -27$  quasar SDSS J1253+6817 at  $z_{\text{em}} = 3.4753$  requires  $t_{\text{on}} > 1 \text{ Myr}$



irrespective of the He II fraction. This again highlights the sensitivity of our measured He II proximity zone sizes to the quasar on-time.

## 5.2 Constraints on the quasar on-time

Figure 8 shows the MCMC estimates of the quasar on-time posterior PDFs marginalized over the initial He II fraction for the 16 remaining  $z_{\text{em}} < 3.6$  quasars excluding HE 2347–4342. Most PDFs are based on  $\sim 130,000$  posterior samples depending on the width of the PDF. Many PDFs are  $\gg 0$  at the upper or lower limit of our flat logarithmic prior on the quasar on-time  $0.01 \text{ Myr} \leq t_{\text{on}} \leq 100 \text{ Myr}$ . Because the lower limit of our prior is physically motivated by the H I proximity effect, while the flatness of the posterior at  $t_{\text{on}} \geq 30 \text{ Myr}$  is effectively determined by the equilibration time-scale, some of these posterior PDFs provide only limited constraints on  $t_{\text{on}}$ . Specifically, if the posterior at  $t_{\text{on}} = 0.01 \text{ Myr}$  is  $> 10$  per cent of its maximum, we quote a  $1\sigma$  upper limit on  $t_{\text{on}}$  as the 84th percentile of the posterior. Likewise, if the posterior at  $t_{\text{on}} = 100 \text{ Myr}$  is  $> 10$  per cent of its maximum, we define a  $1\sigma$  lower limit on  $t_{\text{on}}$  as the 16th percentile of the posterior. For the remaining quasars we quote the median of the posterior as a measurement of  $t_{\text{on}}$  with a  $1\sigma$  equal-tailed credibility interval derived from the 16th and the 84th percentile of the posterior, respectively.

The upper panel of Fig. 8 shows the  $t_{\text{on}}$  posteriors of the five quasars from Table 1 whose  $R_{\text{pz}}$  values are highly uncertain due to C IV redshift errors. Large redshift errors significantly broaden the model  $R_{\text{sim}}$  distributions and result in weak constraints on  $t_{\text{on}}$ , similar to four quasars from Paper I. According to the above definition, we obtain  $1\sigma$  upper limits on  $t_{\text{on}}$ . Quasars with more precise redshifts ( $\sigma_v \leq 400 \text{ km s}^{-1}$ ) have significantly narrower  $t_{\text{on}}$  posteriors, except SDSS J1237+0126 whose He II proximity zone size may have been underestimated (Section 3). For four quasars we obtain lower limits on the quasar on-time (middle panel of Fig. 8) due to their combination of a large proximity zone and moderate to low luminosity (PC 0058+0215). The bottom panel in Fig. 8 shows the  $t_{\text{on}}$  posteriors of the six quasars for which we obtain individual on-time measurements. Their posteriors span distinct ranges in  $t_{\text{on}}$ , indicating an intrinsically broad distribution of quasar on-times from  $\lesssim 1 \text{ Myr}$  to  $\sim 10 \text{ Myr}$ . The precision of the measurements ranges from 0.28 dex (HS 1700+6416) to 0.48 dex (HS 0911+4809), which mainly reflects the redshift precision. On-times of up to  $\approx 10 \text{ Myr}$  can be measured securely, but for longer on-times the flat tail due to the finite equilibration timescale becomes stronger, eventually resulting in lower limits on the on-time. Both the middle and lower panels show that with sufficiently precise redshifts, He II proximity zones constrain individual on-times from  $\approx 1 \text{ Myr}$  up to the He II equilibration time of  $\sim 30 \text{ Myr}$ , which sets the physical limit of the method.

In Fig. 9 we plot the inferred quasar on-times or limits thereof as a function of quasar absolute magnitude. We also show the results for the six  $z_{\text{em}} > 3.6$  quasars from Paper I with updated inferences based on our extended model grid and adjusted to our different definition of limits on  $t_{\text{on}}$ . There is strong diversity in the quasar on-times with no obvious dependence on absolute magnitude. This is similar to the lack of a trend in  $R_{\text{pz}}(M_{1450})$  in Fig. 6, but now we account for the redshift dependence and provide quantitative constraints on  $t_{\text{on}}$  based on the observed scatter of He II proximity zone sizes.

## 5.3 No dependence of quasar on-time on black hole mass and Eddington ratio

Figure 10 shows the quasar on-time as a function of black hole mass for the 13 quasars for which both quantities are available (Table 3

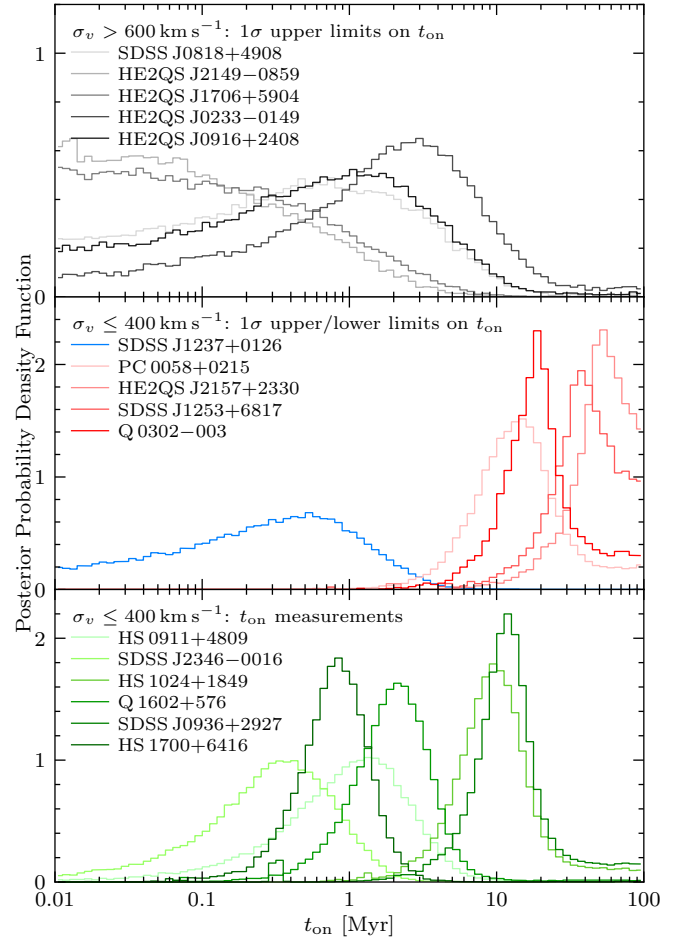


**Figure 8.** MCMC estimates of the posterior PDFs of the quasar on-time  $t_{\text{on}}$  marginalized over the initial He II fraction for the 16 newly reported  $z_{\text{em}} < 3.6$  quasars (Table 1). The posteriors are grouped by their shape and by quasar redshift error that determine the sensitivity of  $R_{\text{pz}}$  to  $t_{\text{on}}$ . The colour coding distinguishes  $t_{\text{on}}$  posteriors for quasars with uncertain C IV redshifts (grey tones), and more precise redshifts yielding upper limits (blue), lower limits (red tones) and measurements (green tones) for  $t_{\text{on}}$ , respectively.

excluding HE 2347–4342). In the range of black hole mass spanned by our sample ( $M_{\text{BH}} \approx 10^9\text{--}10^{10} M_{\odot}$ ) both quantities do not correlate, although the  $\pm 0.55$  dex systematic uncertainty in the virial black hole masses significantly contributes to the observed scatter. Figure 11 shows the quasar on-time as function of the Eddington ratio  $L_{\text{bol}}/L_{\text{Edd}}$ . The 13 quasars roughly emit at their Eddington limit considering the systematic uncertainty induced by the virial black hole mass measurements (Equation 7). The quasar on-time also does not correlate with the Eddington ratio. The dashed lines in Fig. 11 indicate the  $e$ -folding time-scale for SMBH growth

$$t_S = \frac{c\sigma_T(1-Y/2)}{4\pi Gm_p} \frac{\epsilon}{(1-\epsilon)} \left( \frac{L_{\text{bol}}}{L_{\text{Edd}}} \right)^{-1} \quad (9)$$

$$\approx 397 \text{ Myr} \frac{\epsilon}{(1-\epsilon)} \left( \frac{L_{\text{bol}}}{L_{\text{Edd}}} \right)^{-1}$$

for different radiative efficiencies  $\epsilon$ . For  $\epsilon = 0.1$  (e.g. Yu & Tremaine 2002; Ueda et al. 2014; Shankar et al. 2020) and  $L_{\text{bol}} = L_{\text{Edd}}$  one obtains  $t_S \approx 44 \text{ Myr}$ . This is significantly longer than the on-times  $t_{\text{on}} \lesssim 5 \text{ Myr}$  we infer for half of our sample. Such small  $t_{\text{on}}$  values may indicate episodic quasar lifetimes, i.e. that their SMBHs grew

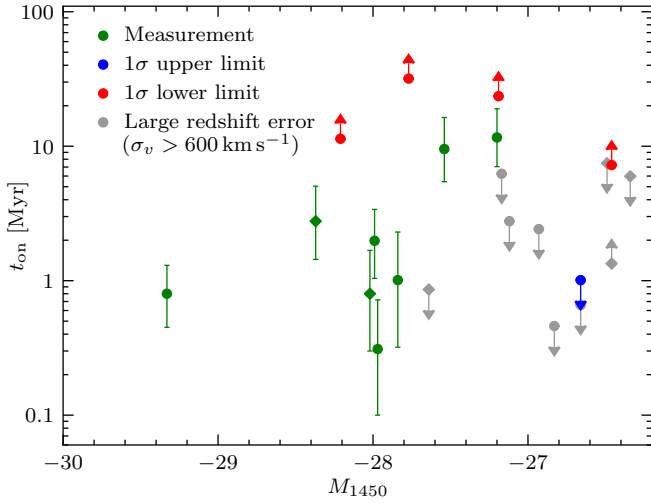


**Figure 9.** Inferred quasar on-time  $t_{\text{on}}$  as a function of absolute magnitude  $M_{1450}$  for the 22 quasars in our combined sample. Green symbols show  $t_{\text{on}}$  measurements (posterior median with 16–84th percentile range from Fig. 8), while blue and red symbols mark  $1\sigma$  upper limits (84th percentile of the posterior) and  $1\sigma$  lower limits (16th percentile of the posterior) for quasars with precise systemic redshifts ( $\sigma_v \leq 400 \text{ km s}^{-1}$ ), respectively. Limits derived for quasars with larger redshift errors are shown in grey.

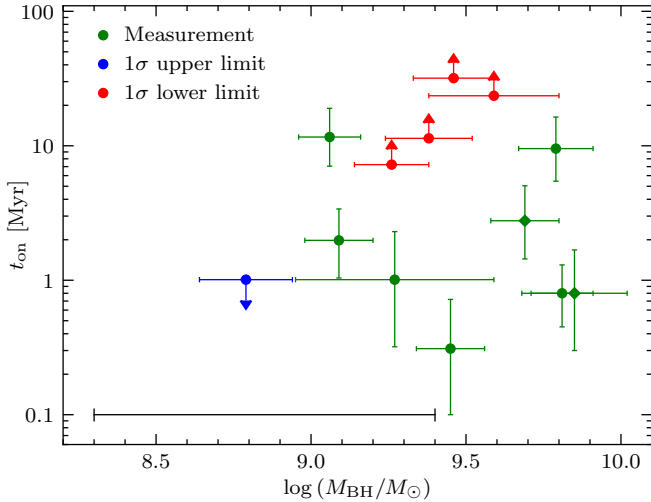


**Figure 10.** Inferred quasar on-time  $t_{\text{on}}$  as a function of black hole mass  $M_{\text{BH}}$  for 13 He II-transparent quasars (Table 3 excluding HE 2347–4342). Quasar on-time measurements and limits are labelled as in Fig. 9. Individual error bars are  $1\sigma$  statistical errors, while the bottom bar indicates the  $\pm 0.55$  dex systematic uncertainty in  $M_{\text{BH}}$ .

in short bursts with  $t_Q \ll t_S$ . Unless most of our observed quasars are radiatively inefficient ( $\epsilon \ll 0.1$ , e.g. Volonteri et al. 2015; Davies et al. 2019), their short on-times imply a small mass growth by  $\lesssim 10$  per cent in the current quasar episode. However, the occurrence of lower limits  $t_{\text{on}} \gtrsim 10 \text{ Myr}$  indicates that not all quasar episodes are that short, so the He II proximity zones may sample a possibly very broad distribution of quasar lifetimes (Khrykin et al. 2021).

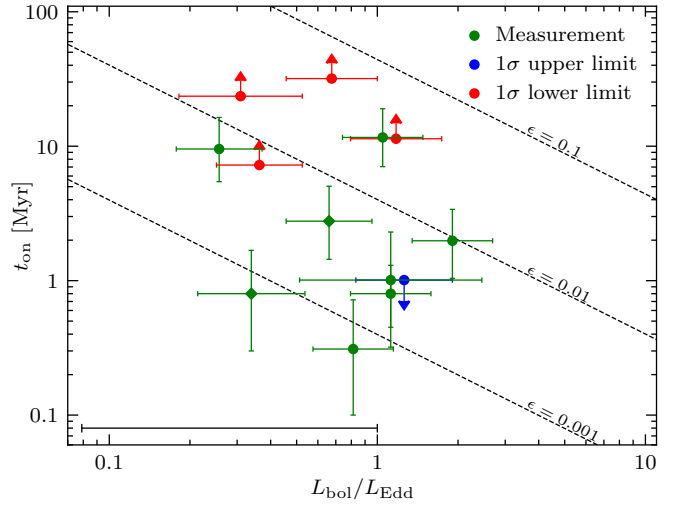


**Figure 11.** Inferred quasar on-time  $t_{\text{on}}$  as a function of Eddington ratio  $L_{\text{bol}}/L_{\text{Edd}}$  for 13 He II-transparent quasars (Table 3 excluding HE 2347–4342). Quasar on-time measurements and limits are labelled as in Fig. 9. Individual error bars are  $1\sigma$  statistical errors, while the bottom bar indicates the  $\pm 0.55$  dex systematic uncertainty in  $L_{\text{bol}}/L_{\text{Edd}}$ . The dashed lines show the  $e$ -folding time-scale of SMBH growth for different radiative efficiencies  $\epsilon$ .

## 6 DISCUSSION

### 6.1 Dependence on the He II fraction prior

The inferred quasar on-times depend on the assumed prior on the initial He II fraction in the surrounding IGM. Similar to Paper I, we adopted a uniform prior  $0.01 \leq x_{\text{He II},0} \leq 1$  to reflect the considerable uncertainty in the local ionization conditions during He II reionization. The measured large-scale He II absorption indicates a low median He II fraction of 2–3 per cent at  $z \approx 3.1$  (Khrykin et al. 2016; Worseck et al. 2019) with spatial variations that are consistent with semi-numerical models of a fluctuating He II-ionizing background after He II reionization (Davies & Furlanetto 2014; Davies et al. 2017). However, the parameters of these models are not well constrained by measurements of the He II effective optical depth, such that the spatial distribution of the He II fraction is still uncertain.

In order to explore how our results change with the  $x_{\text{He II},0}$  prior, we repeated the analysis with a restricted uniform prior  $0.01 \leq x_{\text{He II},0} \leq 0.05$  that is consistent with the inferences from the He II Ly $\alpha$  absorption at  $2.8 < z < 3.3$  (Worseck et al. 2019). In Figure 12 we compare the resulting posterior PDFs for  $t_{\text{on}}$  to the ones from Section 5.2 for the 13 quasars with precisely measured He II proximity zone sizes based on their precise systemic redshifts ( $\sigma_v \leq 400 \text{ km s}^{-1}$ ). Table 4 compares the on-times for all 22 quasars whose He II proximity zone sizes are not significantly negative, and therefore allow us to constrain  $t_{\text{on}}$  (Table 1 excluding HE 2347–4342 and HE2QS J2354–2033). Due to the fewer ionizing photons required to create a large proximity zone, the posterior PDFs shift to lower values, in agreement with the credible regions for the unrestricted prior at low  $x_{\text{He II},0}$  (Fig. 5). Upper and lower  $1\sigma$  limits on  $t_{\text{on}}$  decrease by  $\approx 0.4$  dex and  $\approx 0.5$  dex, respectively. The eight  $t_{\text{on}}$  measurements also shift to lower values by  $\approx 0.5$  dex, resulting in three more limits due to the decreasing ratio between the peak of the posterior and its tail at 100 Myr according to the definition in Section 5.2. Nevertheless, we still infer a broad range in  $t_{\text{on}}$  from  $\lesssim 0.3$  to  $\gtrsim 10 \text{ Myr}$ . Our constraints can be improved either by more

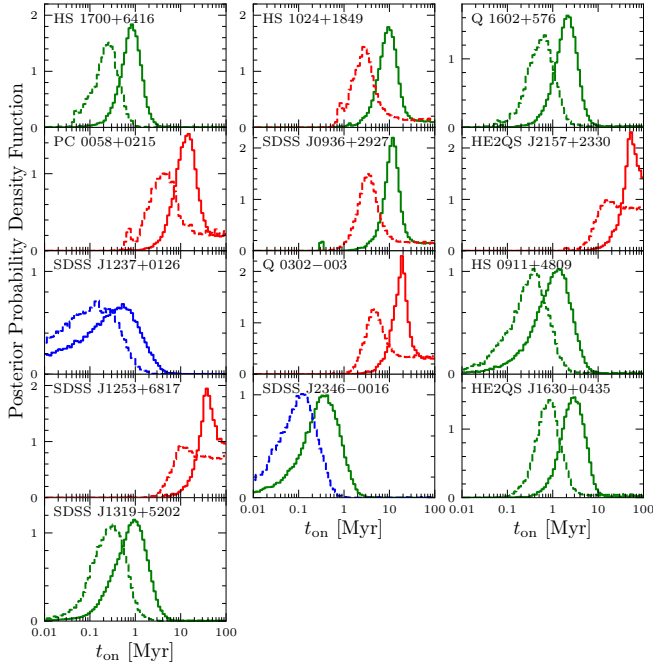


**Figure 12.** MCMC estimates of the posterior PDFs of the quasar on-time  $t_{\text{on}}$  for two uniform priors  $0.01 \leq x_{\text{He II},0} \leq 1$  (solid, Fig. 8) and  $0.01 \leq x_{\text{He II},0} \leq 0.05$  (dashed) for the 13 quasars with precise systemic redshifts ( $\sigma_v \leq 400 \text{ km s}^{-1}$ ). The colours indicate PDFs resulting in  $t_{\text{on}}$  measurements (green),  $1\sigma$  upper limits (blue), and  $1\sigma$  lower limits (red).

**Table 4.** On-times  $t_{\text{on}}$  for the 22 quasars considered in this work for two different uniform priors on the initial IGM He II fraction  $x_{\text{He II},0}$ .

Quasar	$0.01 \leq x_{\text{He II},0} \leq 1$ $t_{\text{on}}$ [Myr]	$0.01 \leq x_{\text{He II},0} \leq 0.05$ $t_{\text{on}}$ [Myr]
HE2QS J2149-0859	< 0.46	< 0.18
HE2QS J1706+5904	< 0.66	< 0.28
SDSS J1237+0126	< 1.01	< 0.36
SDSS J2346-0016	$0.31^{+0.41}_{-0.21}$	< 0.22
SDSS J0818+4908	< 2.42	< 0.88
HE2QS J0916+2408	< 2.77	< 1.02
HS 0911+4809	$1.01^{+1.29}_{-0.69}$	$0.31^{+0.44}_{-0.22}$
HE2QS J0233-0149	< 6.24	< 2.36
Q 1602+576	$1.98^{+1.41}_{-0.94}$	$0.56^{+0.53}_{-0.30}$
PC 0058+0215	> 7.24	> 2.05
HS 1700+6416	$0.80^{+0.50}_{-0.35}$	$0.23^{+0.18}_{-0.12}$
SDSS J0936+2927	$11.62^{+7.37}_{-4.57}$	> 2.11
HS 1024+1849	$9.53^{+6.83}_{-4.08}$	> 1.52
SDSS J1253+6817	> 23.55	> 8.22
Q 0302-003	> 11.36	> 3.33
HE2QS J2157+2330	> 31.84	> 10.87
HE2QS J2311-1417	< 0.86	< 0.29
SDSS J1614+4859	< 5.98	< 2.89
SDSS J1711+6052	< 7.48	< 3.66
SDSS J1319+5202	$0.80^{+0.88}_{-0.50}$	$0.26^{+0.31}_{-0.16}$
SDSS J1137+6237	> 1.34	> 0.71
HE2QS J1630+0435	$2.77^{+2.27}_{-1.33}$	$0.82^{+0.83}_{-0.40}$

precise systemic redshifts from CO or [C II]  $158 \mu\text{m}$  emission from the quasar host galaxies covered at mm to sub-mm wavelengths, or via better priors on  $x_{\text{He II},0}$  from semi-numerical models of the fluctuating UV background at the end of He II reionization (Davies et al. 2017) which is left to future work.

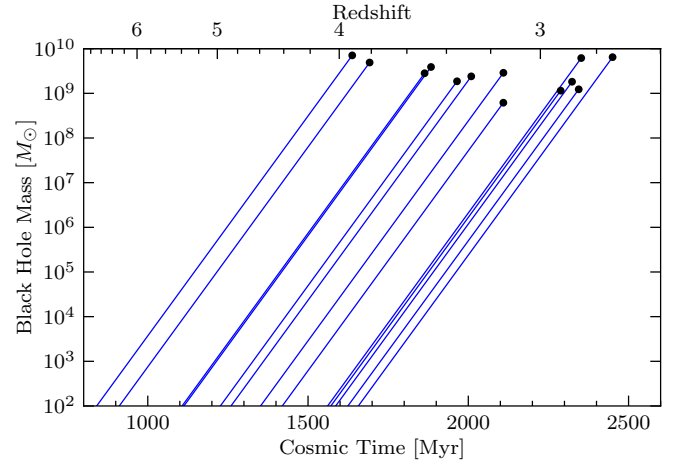


**Figure 13.** SMBH growth histories of the 13 He II-transparent quasars with on-time constraints and measured black hole masses (circles). The lines show their exponential growth history assuming  $\epsilon = 0.1$  and a constant Eddington ratio  $L_{\text{bol}}/L_{\text{Edd}} = 1$ .

## 6.2 Implications for SMBH growth

Here we consider the implications of our inferred quasar on-times for the growth histories of their SMBHs to their measured masses. In our modelling we assumed that each quasar shone at a constant “light bulb” luminosity  $L_{\text{bol}}$  for the time  $t_{\text{on}}$  prior to our observation. Because the inferred on-times are generally much smaller than the Salpeter time, the light bulb model is still a good approximation to the standard model of exponential mass growth<sup>7</sup>

$$M_{\text{BH}}(t) = M_{\text{seed}} e^{(t-t_{\text{seed}})/t_S} \quad (10)$$

for a black hole with a constant radiative efficiency and Eddington ratio that had a seed mass  $M_{\text{seed}}$  at some cosmic time  $t_{\text{seed}}$ . Figure 13 illustrates the exponential growth scenario for the 13 He II-transparent quasars with on-time constraints and estimated black hole masses. The growth times  $t_{\text{gr}} = t - t_{\text{seed}}$  from a stellar remnant seed mass  $\sim 100 M_{\odot}$  are  $t_{\text{gr}} \sim 700 \text{ Myr}$ , and for continuous unobscured SMBH growth these would be equal to the on-times  $t_{\text{on}}$ . For about half of our sample (7 out of 13) the on-times inferred from the He II proximity zone sizes ( $t_{\text{on}} \lesssim 5 \text{ Myr}$ ) are considerably shorter than the Salpeter time  $t_S \ll t_{\text{gr}}$ , implying SMBH growth during episodic quasar activity and/or in obscured phases.

Episodic quasar activity on a wide range of time-scales has been predicted by many models of quasar and black hole co-evolution (e.g. Ciotti & Ostriker 2001; Hopkins et al. 2006; Novak et al. 2011; Anglés-Alcázar et al. 2017). Consider for simplicity a “blinking light bulb” model in which every quasar episode of  $t_Q = 20 \text{ Myr}$  is followed by a quiescent phase of  $t_{\text{off}} = 30 \text{ Myr}$ . In this case, our observations sample random times  $t_{\text{on}} \leq t_Q$ , and after each quasar episode the surrounding IGM will re-equilibrate to the He II fraction implied by the UV background ( $t_{\text{eq}} \approx \Gamma_{\text{He II}}^{-1} \approx 10\text{--}30 \text{ Myr}$  at the redshifts of interest), causing the proximity zone to disappear. If the SMBHs grow exponentially, but not in the quiescent phases, the required time  $t_{\text{blink}} = t_{\text{gr}}(t_Q + t_{\text{off}})/t_Q \sim 1750 \text{ Myr}$  is barely sufficient to explain the SMBH masses in Fig. 13. Quasars would have to blink over the

<sup>7</sup> For exponential growth at constant Eddington ratio, Equations (7) and (10) imply that during  $t_{\text{on}}$  the quasar absolute magnitude increases by  $\Delta M_{1450} \approx 1.19 t_{\text{on}}/t_S$ , which is small for most quasars in our sample.

age of the Universe to acquire their black hole masses. The problem is exacerbated by shorter quasar lifetimes implied at lower initial He II fractions in the end stages of He II reionization (Section 6.1). This indicates that either the off-times must be shorter than the equilibration time, such that the proximity zones do not disappear (see Davies et al. 2020 for the similar case of  $z \sim 6$  H I proximity zones) or that black holes continue to grow in obscured phases, i.e. during  $t_{\text{off}}$ . X-ray-selected samples of Active Galactic Nuclei (AGN) revealed that the fraction of Compton-thin (equivalent line-of-sight hydrogen column density  $N_{\text{H}} = 10^{22}-10^{24} \text{ cm}^{-2}$ ) obscured AGN depends on X-ray luminosity and redshift (e.g. Merloni et al. 2014; Ueda et al. 2014; Buchner et al. 2015; Aird et al. 2015). While at  $z \sim 2$  the obscured fraction decreases with luminosity from  $\sim 70$  per cent to  $\sim 30$  per cent (Ueda et al. 2014; Aird et al. 2015), at  $z \sim 3$  the obscured fraction is  $\sim 60$  per cent independent of luminosity (Buchner et al. 2015; Aird et al. 2015), possibly increasing further toward higher redshifts (Vito et al. 2018). It is therefore plausible that much of the mass growth occurred when the SMBH was obscured by gas and dust, such that SMBH mass and the duration of the UV-luminous quasar phase are uncorrelated. We will consider more complex lightcurves than the simple light bulb model in future work.

## 7 CONCLUSIONS

We have used a sample of  $17.2.74 < z_{\text{em}} < 3.51$  He II-transparent quasars with science-grade ( $S/N \gtrsim 3$ ) *HST*/COS spectra (Worseck et al. 2019) to measure the sizes of their highly ionized He II proximity zones. Given that these zones typically span only a few pMpc, precise measurements are often hampered by quasar redshift error. Therefore, we obtained ancillary near-infrared spectroscopy to measure accurate and precise systemic redshifts of 12 quasars from low-ionization UV and optical emission lines (Mg II, H $\beta$ , [O III]) that also allow for estimates of the quasar black hole masses and Eddington ratios. Together with two  $z_{\text{em}} > 3.6$  quasars from Paper I and excluding the peculiar quasar HE 2347–4342 (e.g. Reimers et al. 1997), we have compiled the first statistical sample of 13 quasars with accurate and precise He II proximity zone sizes ( $\sigma_{R_{\text{pz}}} \lesssim 1 \text{ pMpc}$ ). Our main results are the following:

- (i) He II proximity zone sizes span a large range  $2 \text{ pMpc} \lesssim R_{\text{pz}} \lesssim 15 \text{ pMpc}$ . Nine out of 13 quasars with precise systemic redshifts have  $R_{\text{pz}} > 5 \text{ pMpc}$ , suggesting that large proximity zones are common, and that quasar redshift error significantly limits further use of the remaining He II-transparent quasars.
- (ii) He II proximity zone sizes do not correlate with quasar UV luminosity or redshift (Figs. 6 and 7). Given their weak sensitivity to the He II fraction in the ambient IGM (Khrykin et al. 2016, 2019), the factor  $\sim 5$  spread of  $R_{\text{pz}}$  at similar luminosity is mainly due to variations in the individual quasar on-time, but variations in the He II fraction due to patchy He II reionization and IGM density fluctuations contribute as well.
- (iii) Exploiting the sensitivity of  $R_{\text{pz}}$  to quasar on-times  $t_{\text{on}}$  shorter than the equilibration time of He II in the ambient IGM  $t_{\text{eq}} = 10\text{--}30 \text{ Myr}$  at these redshifts (Khrykin et al. 2016; Worseck et al. 2019) we have inferred individual quasar on-times using our Bayesian framework developed in Paper I. The 13 quasars with precise He II proximity zone sizes span a large range in on-time from  $t_{\text{on}} \lesssim 1 \text{ Myr}$  to  $t_{\text{on}} > 30 \text{ Myr}$ , larger than the typical  $\pm 0.3 \text{ dex}$  statistical uncertainty due to remaining redshift error, the IGM density field, and the initial He II fraction prior to quasar activity.
- (iv) The quasar on-time neither correlates with quasar luminos-

ity (Fig. 9), nor with black hole mass (Fig. 10) or Eddington ratio (Fig. 11).

The predominantly short quasar on-times  $t_{\text{on}} < 10 \text{ Myr}$  and the lack of correlation with the black hole properties suggest that our observations sample the distribution of episodic quasar lifetimes. Unless these quasars are radiatively highly inefficient (Davies et al. 2019), their black holes must have grown in bursts significantly shorter than the  $e$ -folding time-scale  $t_{\text{S}} \sim 44 \text{ Myr}$ . Such short quasar lifetimes suggest a long quasar duty cycle that is, however, not well constrained given the age of the Universe at  $z < 4$  ( $> 1.6 \text{ Gyr}$ ). This is different to the situation for  $z \gtrsim 6$  H I proximity zones that are insensitive to quasar on-times  $t_{\text{on}} \gtrsim 0.1 \text{ Myr}$  (Eilers et al. 2017, 2018; Davies et al. 2020), but probe the growth of SMBHs  $\lesssim 1 \text{ Gyr}$  after the Big Bang. If SMBHs of quasars at  $z \sim 6$  accreted similarly to their counterparts at  $z \sim 3$ , most of their mass must have been built up during phases of obscuration or radiative inefficiency.

The sensitivity of individual He II proximity zones to the time-scale of prior quasar activity of up to  $\sim 30 \text{ Myr}$  offers a unique opportunity to constrain the underlying distribution of episodic quasar lifetimes (Khrykin et al. 2021), which can be compared to predictions from models of galaxy and black hole co-evolution. Moreover, we anticipate to more than double the sample of He II-transparent quasars with precise systemic redshifts in our ongoing joint programme with *HST*/COS and Gemini/GNIRS (PI Worseck) to further resolve quasar activity on time-scales of several tens of Myr.

## ACKNOWLEDGEMENTS

We would like to thank Robert Simcoe for sharing his reduced near-infrared spectrum of HE 2347–4342 and Feige Wang for his Python code to fit the near-infrared spectra. We would also like to thank Anna-Christina Eilers and Frederick Davies for valuable discussions.

GW has been partially supported by the Deutsches Zentrum für Luft- und Raumfahrt (DLR) grant 50OR1720. ISK acknowledges support from the grant of the Russian Foundation for Basic Research (RFBR) No. 18-32-00798.

This work is partly based on observations obtained at the Hale Telescope, Palomar Observatory as part of a continuing collaboration between the California Institute of Technology, NASA Jet Propulsion Laboratory, Yale University, and the National Astronomical Observatories of China. This material is based upon work supported by the Association of Universities for Research in Astronomy (AURA) through the National Science Foundation under AURA Cooperative Agreement AST 0132798 as amended.

The LBT is an international collaboration among institutions in the United States, Italy and Germany. LBT Corporation partners are: The University of Arizona on behalf of the Arizona Board of Regents; Istituto Nazionale di Astrofisica, Italy; LBT Beteiligungsgesellschaft, Germany, representing the Max-Planck Society, The Leibniz Institute for Astrophysics Potsdam, and Heidelberg University; The Ohio State University, and The Research Corporation, on behalf of The University of Notre Dame, University of Minnesota and University of Virginia.

This work is partly based on observations collected at the European Southern Observatory under ESO programme 290.A-5094.

This work is partly based on observations collected at the Centro Astronómico Hispano Alemán (CAHA) at Calar Alto, operated jointly by the Max Planck Institute for Astronomy and the Instituto de Astrofísica de Andalucía (CSIC).

This work is partly based on data obtained from Lick Observatory, owned and operated by the University of California.



Some of the data presented herein were obtained at the W. M. Keck Observatory, which is operated as a scientific partnership among the California Institute of Technology, the University of California and the National Aeronautics and Space Administration. The Observatory was made possible by the generous financial support of the W. M. Keck Foundation. The authors wish to recognize and acknowledge the very significant cultural role and reverence that the summit of Mauna Kea has always had within the indigenous Hawaiian community. We are most fortunate to have the opportunity to conduct observations from this mountain.

This research has made use of the Keck Observatory Archive (KOA), which is operated by the W. M. Keck Observatory and the NASA Exoplanet Science Institute (NExScI), under contract with the National Aeronautics and Space Administration. Some data presented in this work were obtained from the Keck Observatory Database of Ionized Absorbers toward Quasars (KODIAQ), which was funded through NASA ADAP grant NNX10AE84G.

This paper includes data gathered with the 6.5 m Magellan Telescopes located at Las Campanas Observatory, Chile.

Funding for the Sloan Digital Sky Survey IV has been provided by the Alfred P. Sloan Foundation, the U.S. Department of Energy Office of Science, and the Participating Institutions. SDSS-IV acknowledges support and resources from the Center for High-Performance Computing at the University of Utah. The SDSS web site is [www.sdss.org](http://www.sdss.org). SDSS-IV is managed by the Astrophysical Research Consortium for the Participating Institutions of the SDSS Collaboration including the Brazilian Participation Group, the Carnegie Institution for Science, Carnegie Mellon University, the Chilean Participation Group, the French Participation Group, Harvard-Smithsonian Center for Astrophysics, Instituto de Astrofísica de Canarias, The Johns Hopkins University, Kavli Institute for the Physics and Mathematics of the Universe (IPMU) / University of Tokyo, the Korean Participation Group, Lawrence Berkeley National Laboratory, Leibniz Institut für Astrophysik Potsdam (AIP), Max-Planck-Institut für Astronomie (MPIA Heidelberg), Max-Planck-Institut für Astrophysik (MPA Garching), Max-Planck-Institut für Extraterrestrische Physik (MPE), National Astronomical Observatories of China, New Mexico State University, New York University, University of Notre Dame, Observatório Nacional / MCTI, The Ohio State University, Pennsylvania State University, Shanghai Astronomical Observatory, United Kingdom Participation Group, Universidad Nacional Autónoma de México, University of Arizona, University of Colorado Boulder, University of Oxford, University of Portsmouth, University of Utah, University of Virginia, University of Washington, University of Wisconsin, Vanderbilt University, and Yale University.

The Pan-STARRS1 Surveys (PS1) and the PS1 public science archive have been made possible through contributions by the Institute for Astronomy, the University of Hawaii, the Pan-STARRS Project Office, the Max-Planck Society and its participating institutes, the Max Planck Institute for Astronomy, Heidelberg and the Max Planck Institute for Extraterrestrial Physics, Garching, The Johns Hopkins University, Durham University, the University of Edinburgh, the Queen's University Belfast, the Harvard-Smithsonian Center for Astrophysics, the Las Cumbres Observatory Global Telescope Network Incorporated, the National Central University of Taiwan, the Space Telescope Science Institute, the National Aeronautics and Space Administration under Grant No. NNX08AR22G issued through the Planetary Science Division of the NASA Science Mission Directorate, the National Science Foundation Grant No. AST-1238877, the University of Maryland, Eotvos Lorand University (ELTE), the Los Alamos National Laboratory, and the Gordon and Betty Moore Foundation.

This research made use of ASTROPY (Astropy Collaboration et al. 2013, 2018), NUMPY (van der Walt et al. 2011) and MATPLOTLIB (Hunter 2007).

## DATA AVAILABILITY

The data underlying this article will be shared on reasonable request to the corresponding author.

## REFERENCES

- Abolfathi B., et al., 2018, *ApJS*, **235**, 42
- Adelberger K. L., Steidel C. C., 2005, *ApJ*, **630**, 50
- Adelberger K. L., Steidel C. C., Kollmeier J. A., Reddy N. A., 2006, *ApJ*, **637**, 74
- Aird J., Coil A. L., Georgakakis A., Nandra K., Barro G., Pérez-González P. G., 2015, *MNRAS*, **451**, 1892
- Alam S., et al., 2015, *ApJS*, **219**, 12
- Anderson S. F., Hogan C. J., Williams B. F., Carswell R. F., 1999, *AJ*, **117**, 56
- Anglés-Alcázar D., Özel F., Davé R., 2013, *ApJ*, **770**, 5
- Anglés-Alcázar D., Faucher-Giguère C.-A., Quataert E., Hopkins P. F., Feldmann R., Torrey P., Wetzel A., Kereš D., 2017, *MNRAS*, **472**, L109
- Anglés-Alcázar D., et al., 2020, arXiv e-prints, [p. arXiv:2008.12303](https://arxiv.org/abs/2008.12303)
- Arrighi Battaia F., Prochaska J. X., Hennawi J. F., Obreja A., Buck T., Cantalupo S., Dutton A. A., Macciò A. V., 2018, *MNRAS*, **473**, 3907
- Astropy Collaboration et al., 2013, *A&A*, **558**, A33
- Astropy Collaboration et al., 2018, *AJ*, **156**, 123
- Bañados E., et al., 2018, *Nature*, **553**, 473
- Bahk H., Woo J.-H., Park D., 2019, *ApJ*, **875**, 50
- Bajtlik S., Duncan R. C., Ostriker J. P., 1988, *ApJ*, **327**, 570
- Baldwin J. A., 1977, *ApJ*, **214**, 679
- Becker G. D., Bolton J. S., 2013, *MNRAS*, **436**, 1023
- Bolton J. S., Haehnelt M. G., 2007, *MNRAS*, **374**, 493
- Borisova E., Lilly S. J., Cantalupo S., Prochaska J. X., Rakic O., Worseck G., 2016, *ApJ*, **830**, 120
- Boroson T., 2005, *AJ*, **130**, 381
- Bournaud F., Dekel A., Teyssier R., Cacciato M., Daddi E., Juneau S., Shankar F., 2011, *ApJ*, **741**, L33
- Buchner J., et al., 2015, *ApJ*, **802**, 89
- Cai Z., et al., 2017, *ApJ*, **837**, 71
- Calverley A. P., Becker G. D., Haehnelt M. G., Bolton J. S., 2011, *MNRAS*, **412**, 2543
- Cantalupo S., Lilly S. J., Haehnelt M. G., 2012, *MNRAS*, **425**, 1992
- Cantalupo S., Arrighi-Battaia F., Prochaska J. X., Hennawi J. F., Madau P., 2014, *Nature*, **506**, 63
- Capelo P. R., Volonteri M., Dotti M., Bellovary J. M., Mayer L., Governato F., 2015, *MNRAS*, **447**, 2123
- Carilli C. L., et al., 2010, *ApJ*, **714**, 834
- Chambers K. C., et al., 2016, arXiv e-prints, [p. arXiv:1612.05560](https://arxiv.org/abs/1612.05560)
- Ciotti L., Ostriker J. P., 2001, *ApJ*, **551**, 131
- Coatman L., Hewett P. C., Banerji M., Richards G. T., Hennawi J. F., Prochaska J. X., 2017, *MNRAS*, **465**, 2120
- Croft R. A. C., 2004, *ApJ*, **610**, 642
- Croom S. M., et al., 2005, *MNRAS*, **356**, 415
- Dall'Aglio A., Wisotzki L., Worseck G., 2008, *A&A*, **491**, 465
- Davies F. B., Furlanetto S. R., 2014, *MNRAS*, **437**, 1141
- Davies F. B., Furlanetto S. R., Dixon K. L., 2017, *MNRAS*, **465**, 2886
- Davies F. B., Hennawi J. F., Eilers A.-C., 2019, *ApJ*, **884**, L19
- Davies F. B., Hennawi J. F., Eilers A.-C., 2020, *MNRAS*, **493**, 1330
- De Rosa G., et al., 2014, *ApJ*, **790**, 145
- Di Matteo T., Springel V., Hernquist L., 2005, *Nature*, **433**, 604
- Di Matteo T., Khandai N., DeGraf C., Feng Y., Croft R. A. C., Lopez J., Springel V., 2012, *ApJ*, **745**, L29
- Eftekharzadeh S., et al., 2015, *MNRAS*, **453**, 2779

- Eilers A.-C., Davies F. B., Hennawi J. F., Prochaska J. X., Lukić Z., Mazzucchelli C., 2017, *ApJ*, **840**, 24
- Eilers A.-C., Hennawi J. F., Davies F. B., 2018, *ApJ*, **867**, 30
- Eilers A.-C., et al., 2020, *ApJ*, **900**, 37
- Fan X., et al., 2006, *AJ*, **132**, 117
- Farina E. P., et al., 2019, *ApJ*, **887**, 196
- Faucher-Giguère C.-A., 2020, *MNRAS*, **493**, 1614
- Fechner C., Reimers D., 2007, *A&A*, **461**, 847
- Fechner C., Baade R., Reimers D., 2004, *A&A*, **418**, 857
- Fletcher T. J., Tang M., Robertson B. E., Nakajima K., Ellis R. S., Stark D. P., Inoue A., 2019, *ApJ*, **878**, 87
- Flewelling H. A., et al., 2020, *ApJS*, **251**, 7
- Foreman-Mackey D., Hogg D. W., Lang D., Goodman J., 2013, *PASP*, **125**, 306
- Gabor J. M., Bournaud F., 2013, *MNRAS*, **434**, 606
- Gallerani S., Ferrara A., Fan X., Choudhury T. R., 2008, *MNRAS*, **386**, 359
- Gaskell C. M., 1982, *ApJ*, **263**, 79
- Gonçalves T. S., Steidel C. C., Pettini M., 2008, *ApJ*, **676**, 816
- Goodman J., Weare J., 2010, *Communications in Applied Mathematics and Computational Science*, **5**, 65
- Grazian A., et al., 2017, *A&A*, **602**, A18
- Green J. C., et al., 2012, *ApJ*, **744**, 60
- Haardt F., Madau P., 2012, *ApJ*, **746**, 125
- Haiman Z., Hui L., 2001, *ApJ*, **547**, 27
- Heap S. R., Williger G. M., Smette A., Hubeny I., Sahu M. S., Jenkins E. B., Tripp T. M., Winkler J. N., 2000, *ApJ*, **534**, 69
- Hennawi J. F., Prochaska J. X., 2007, *ApJ*, **655**, 735
- Hennawi J. F., et al., 2006, *ApJ*, **651**, 61
- Hennawi J. F., Prochaska J. X., Cantalupo S., Arrigoni-Battaia F., 2015, *Science*, **348**, 779
- Herter T. L., et al., 2008, in *Ground-based and Airborne Instrumentation for Astronomy II*. p. 70140X, doi:10.1117/12.789660
- Hewett P. C., Wild V., 2010, *MNRAS*, **405**, 2302
- Ho L. C., Kim M., 2015, *ApJ*, **809**, 123
- Hogan C. J., Anderson S. F., Rugers M. H., 1997, *AJ*, **113**, 1495
- Hopkins P. F., Hernquist L., 2009, *ApJ*, **698**, 1550
- Hopkins P. F., Quataert E., 2010, *MNRAS*, **407**, 1529
- Hopkins P. F., Hernquist L., Martini P., Cox T. J., Robertson B., Di Matteo T., Springel V., 2005a, *ApJ*, **625**, L71
- Hopkins P. F., Hernquist L., Cox T. J., Di Matteo T., Martini P., Robertson B., Springel V., 2005b, *ApJ*, **630**, 705
- Hopkins P. F., Hernquist L., Cox T. J., Di Matteo T., Robertson B., Springel V., 2006, *ApJS*, **163**, 1
- Hopkins P. F., Hernquist L., Cox T. J., Kereš D., 2008, *ApJS*, **175**, 356
- Hopkins P. F., Torrey P., Faucher-Giguère C.-A., Quataert E., Murray N., 2016, *MNRAS*, **458**, 816
- Hui L., Gnedin N. Y., Zhang Y., 1997, *ApJ*, **486**, 599
- Hunter J. D., 2007, *Computing in Science and Engineering*, **9**, 90
- Inayoshi K., Haiman Z., Ostriker J. P., 2016, *MNRAS*, **459**, 3738
- Jakobsen P., Jansen R. A., Wagner S., Reimers D., 2003, *A&A*, **397**, 891
- Jiang L., Fan X., Vestergaard M., Kurk J. D., Walter F., Kelly B. C., Strauss M. A., 2007, *AJ*, **134**, 1150
- Johnson J. L., Whalen D. J., Li H., Holz D. E., 2013, *ApJ*, **771**, 116
- Keating L. C., Haehnelt M. G., Cantalupo S., Puchwein E., 2015, *MNRAS*, **454**, 681
- Keel W. C., et al., 2017, *ApJ*, **835**, 256
- Khaire V., 2017, *MNRAS*, **471**, 255
- Khaire V., Srianand R., 2019, *MNRAS*, **484**, 4174
- Khrykin I. S., Hennawi J. F., McQuinn M., Worseck G., 2016, *ApJ*, **824**, 133
- Khrykin I. S., Hennawi J. F., McQuinn M., 2017, *ApJ*, **838**, 96
- Khrykin I. S., Hennawi J. F., Worseck G., 2019, *MNRAS*, **484**, 3897
- Khrykin I. S., Hennawi J. F., Worseck G., Davies F. B., 2021, *MNRAS*, **500**, 1457
- Kirkman D., Tytler D., 2008, *MNRAS*, **391**, 1457
- Kormendy J., Ho L. C., 2013, *ARA&A*, **51**, 511
- Kormendy J., Richstone D., 1995, *ARA&A*, **33**, 581
- Kulkarni G., Worseck G., Hennawi J. F., 2019, *MNRAS*, **488**, 1035
- Kurk J. D., et al., 2007, *ApJ*, **669**, 32
- LaMassa S. M., et al., 2015, *ApJ*, **800**, 144
- Lidz A., McQuinn M., Zaldarriaga M., Hernquist L., Dutta S., 2007, *ApJ*, **670**, 39
- Liske J., Williger G. M., 2001, *MNRAS*, **328**, 653
- Lusso E., Worseck G., Hennawi J. F., Prochaska J. X., Vignali C., Stern J., O'Meara J. M., 2015, *MNRAS*, **449**, 4204
- Lusso E., Fumagalli M., Rafelski M., Neeleman M., Prochaska J. X., Hennawi J. F., O'Meara J. M., Theuns T., 2018, *ApJ*, **860**, 41
- Lynden-Bell D., 1969, *Nature*, **223**, 690
- MacLeod C. L., et al., 2016, *MNRAS*, **457**, 389
- Madau P., Haardt F., Dotoli M., 2014, *ApJ*, **784**, L38
- Marconi A., Risaliti G., Gilli R., Hunt L. K., Maiolino R., Salvati M., 2004, *MNRAS*, **351**, 169
- Marino R. A., et al., 2018, *ApJ*, **859**, 53
- Martini P., 2004, in Ho L. C., ed., *Coevolution of Black Holes and Galaxies*. p. 169 (arXiv:astro-ph/0304009)
- Martini P., Weinberg D. H., 2001, *ApJ*, **547**, 12
- Maselli A., Gallerani S., Ferrara A., Choudhury T. R., 2007, *MNRAS*, **376**, L34
- Maselli A., Ferrara A., Gallerani S., 2009, *MNRAS*, **395**, 1925
- Mazzucchelli C., et al., 2017, *ApJ*, **849**, 91
- McElroy R. E., et al., 2016, *A&A*, **593**, L8
- McLure R. J., Dunlop J. S., 2004, *MNRAS*, **352**, 1390
- Mejía-Restrepo J. E., Trakhtenbrot B., Lira P., Netzer H., Capellupo D. M., 2016, *MNRAS*, **460**, 187
- Mellema G., Iliev I. T., Alvarez M. A., Shapiro P. R., 2006, *NA*, **11**, 374
- Merloni A., et al., 2014, *MNRAS*, **437**, 3550
- Moorwood A., et al., 1998, *The Messenger*, **94**, 7
- Mortlock D. J., et al., 2011, *Nature*, **474**, 616
- Novak G. S., Ostriker J. P., Ciotti L., 2011, *ApJ*, **737**, 26
- O'Meara J. M., et al., 2015, *AJ*, **150**, 111
- Oke J. B., et al., 1995, *PASP*, **107**, 375
- Oppenheimer B. D., Segers M., Schaye J., Richings A. J., Crain R. A., 2018, *MNRAS*, **474**, 4740
- Pacucci F., Volonteri M., Ferrara A., 2015, *MNRAS*, **452**, 1922
- Planck Collaboration et al., 2020, *A&A*, **641**, A6
- Porciani C., Magliocchetti M., Norberg P., 2004, *MNRAS*, **355**, 1010
- Prochaska J. X., Hennawi J. F., 2009, *ApJ*, **690**, 1558
- Prochaska J. X., et al., 2013, *ApJ*, **776**, 136
- Puchwein E., Haardt F., Haehnelt M. G., Madau P., 2019, *MNRAS*, **485**, 47
- Rees M. J., 1984, *ARA&A*, **22**, 471
- Reimers D., Kohler S., Wisotzki L., Groote D., Rodriguez-Pascual P., Wamsteker W., 1997, *A&A*, **327**, 890
- Richards G. T., Vanden Berk D. E., Reichard T. A., Hall P. B., Schneider D. P., SubbaRao M., Thakar A. R., York D. G., 2002, *AJ*, **124**, 1
- Richards G. T., et al., 2011, *AJ*, **141**, 167
- Runnoe J. C., Brotherton M. S., Shang Z., 2012, *MNRAS*, **422**, 478
- Runnoe J. C., et al., 2016, *MNRAS*, **455**, 1691
- Salpeter E. E., 1964, *ApJ*, **140**, 796
- Sanders D. B., Soifer B. T., Elias J. H., Madore B. F., Matthews K., Neugebauer G., Scoville N. Z., 1988, *ApJ*, **325**, 74
- Sartori L. F., et al., 2016, *MNRAS*, **457**, 3629
- Schawinski K., Koss M., Berney S., Sartori L. F., 2015, *MNRAS*, **451**, 2517
- Schindler J.-T., et al., 2020, *ApJ*, **905**, 51
- Schirmer M., et al., 2016, *MNRAS*, **463**, 1554
- Schmidt M., 1963, *Nature*, **197**, 1040
- Schmidt T. M., Worseck G., Hennawi J. F., Prochaska J. X., Crighton N. H. M., 2017, *ApJ*, **847**, 81
- Schmidt T. M., Hennawi J. F., Worseck G., Davies F. B., Lukić Z., Oñorbe J., 2018, *ApJ*, **861**, 122
- Scott J., Bechtold J., Dobrzycki A., Kulkarni V. P., 2000, *ApJS*, **130**, 67
- Seifert W., et al., 2003, in Iye M., Moorwood A. F. M., eds, *Proc. SPIE Vol. 4841, Instrument Design and Performance for Optical/Infrared Ground-based Telescopes*. pp 962–973, doi:10.1117/12.459494
- Shankar F., Salucci P., Granato G. L., De Zotti G., Danese L., 2004, *MNRAS*, **354**, 1020
- Shankar F., et al., 2020, *Nature Astronomy*, **4**, 282
- Shapiro S. L., 2005, *ApJ*, **620**, 59

- Sheinis A. I., Bolte M., Eppe H. W., Kibrick R. I., Miller J. S., Radovan M. V., Bigelow B. C., Sutin B. M., 2002, *PASP*, **114**, 851
- Shen Y., 2013, Bulletin of the Astronomical Society of India, **41**, 61
- Shen Y., 2016, *ApJ*, **817**, 55
- Shen Y., Ho L. C., 2014, *Nature*, **513**, 210
- Shen Y., et al., 2007, *AJ*, **133**, 2222
- Shen Y., et al., 2016, *ApJ*, **831**, 7
- Shen Y., et al., 2019, *ApJ*, **873**, 35
- Shull J. M., Danforth C. W., 2020, *ApJ*, **899**, 163
- Shull J. M., France K., Danforth C. W., Smith B., Tumlinson J., 2010, *ApJ*, **722**, 1312
- Shull J. M., Stevans M., Danforth C. W., 2012, *ApJ*, **752**, 162
- Sijacki D., Springel V., Haehnelt M. G., 2009, *MNRAS*, **400**, 100
- Simcoe R. A., et al., 2008, in Ground-based and Airborne Instrumentation for Astronomy II, p. 70140U, doi:10.1117/12.790414
- Smee S. A., et al., 2013, *AJ*, **146**, 32
- Smette A., Heap S. R., Williger G. M., Tripp T. M., Jenkins E. B., Songaila A., 2002, *ApJ*, **564**, 542
- Soltan A., 1982, *MNRAS*, **200**, 115
- Springel V., 2005, *MNRAS*, **364**, 1105
- Springel V., Di Matteo T., Hernquist L., 2005, *ApJ*, **620**, L79
- Steidel C. C., Shapley A. E., Pettini M., Adelberger K. L., Erb D. K., Reddy N. A., Hunt M. P., 2004, *ApJ*, **604**, 534
- Steidel C. C., Bogosavljević M., Shapley A. E., Reddy N. A., Rudie G. C., Pettini M., Trainor R. F., Strom A. L., 2018, *ApJ*, **869**, 123
- Steinborn L. K., Hirschmann M., Dolag K., Shankar F., Juneau S., Krumpel M., Remus R.-S., Teklu A. F., 2018, *MNRAS*, **481**, 341
- Stern J., Laor A., 2012, *MNRAS*, **426**, 2703
- Stevans M. L., Shull J. M., Danforth C. W., Tilton E. M., 2014, *ApJ*, **794**, 75
- Syphers D., Shull J. M., 2013, *ApJ*, **765**, 119
- Syphers D., Shull J. M., 2014, *ApJ*, **784**, 42
- Syphers D., Anderson S. F., Zheng W., Meiksin A., Haggard D., Schneider D. P., York D. G., 2011a, *ApJ*, **726**, 111
- Syphers D., et al., 2011b, *ApJ*, **742**, 99
- Syphers D., Anderson S. F., Zheng W., Meiksin A., Schneider D. P., York D. G., 2012, *AJ*, **143**, 100
- Tilton E. M., Stevans M. L., Shull J. M., Danforth C. W., 2016, *ApJ*, **817**, 56
- Tody D., 1993, in Hanisch R. J., Brissenden R. J. V., Barnes J., eds, Astronomical Society of the Pacific Conference Series Vol. 52, Astronomical Data Analysis Software and Systems II, p. 173
- Trainor R. F., Steidel C. C., 2012, *ApJ*, **752**, 39
- Trainor R., Steidel C. C., 2013, *ApJ*, **775**, L3
- Tsuzuki Y., Kawara K., Yoshii Y., Oyabu S., Tanabé T., Matsuoka Y., 2006, *ApJ*, **650**, 57
- Tytler D., Fan X.-M., 1992, *ApJS*, **79**, 1
- Ueda Y., Akiyama M., Hasinger G., Miyaji T., Watson M. G., 2014, *ApJ*, **786**, 104
- Vanden Berk D. E., et al., 2001, *AJ*, **122**, 549
- Venemans B. P., et al., 2013, *ApJ*, **779**, 24
- Vestergaard M., Osmer P. S., 2009, *ApJ*, **699**, 800
- Vestergaard M., Peterson B. M., 2006, *ApJ*, **641**, 689
- Vestergaard M., Wilkes B. J., 2001, *ApJS*, **134**, 1
- Vito F., et al., 2018, *MNRAS*, **473**, 2378
- Vogt S. S., et al., 1994, HIRES: the high-resolution echelle spectrometer on the Keck 10-m Telescope, p. 362, doi:10.1117/12.176725
- Volonteri M., Rees M. J., 2005, *ApJ*, **633**, 624
- Volonteri M., Silk J., Dubus G., 2015, *ApJ*, **804**, 148
- Wang F., et al., 2020, *ApJ*, **896**, 23
- Weinberg D. H., Hernquist L., Katz N., Croft R., Miralda-Escudé J., 1997, in Petitjean P., Charlot S., eds, Structure and Evolution of the Intergalactic Medium from QSO Absorption Line System, p. 133 (arXiv:astro-ph/9709303)
- White M., Martini P., Cohn J. D., 2008, *MNRAS*, **390**, 1179
- White M., et al., 2012, *MNRAS*, **424**, 933
- Woo J.-H., Le H. A. N., Karouzos M., Park D., Park D., Malkan M. A., Treu T., Bennert V. N., 2018, *ApJ*, **859**, 138
- Worseck G., Prochaska J. X., 2011, *ApJ*, **728**, 23
- Worseck G., Wisotzki L., 2006, *A&A*, **450**, 495
- Worseck G., Fechner C., Wisotzki L., Dall’Aglio A., 2007, *A&A*, **473**, 805
- Worseck G., Wisotzki L., Selman F., 2008, *A&A*, **487**, 539
- Worseck G., Prochaska J. X., Hennawi J. F., McQuinn M., 2016, *ApJ*, **825**, 144
- Worseck G., Davies F. B., Hennawi J. F., Prochaska J. X., 2019, *ApJ*, **875**, 111
- Wu X.-B., et al., 2015, *Nature*, **518**, 512
- Yang Q., et al., 2018, *ApJ*, **862**, 109
- Yang J., et al., 2020, *ApJ*, **897**, L14
- York D. G., et al., 2000, *AJ*, **120**, 1579
- Yu Q., Tremaine S., 2002, *MNRAS*, **335**, 965
- Zheng W., Syphers D., Meiksin A., Kriss G. A., Schneider D. P., York D. G., Anderson S. F., 2015, *ApJ*, **806**, 142
- Zheng W., Meiksin A., Syphers D., 2019, *ApJ*, **883**, 123
- Zuo W., Wu X.-B., Fan X., Green R., Wang R., Bian F., 2015, *ApJ*, **799**, 189
- van Dokkum P. G., 2001, *PASP*, **113**, 1420
- van der Walt S., Colbert S. C., Varoquaux G., 2011, *Computing in Science and Engineering*, **13**, 22

## APPENDIX A: MOCK *HST*/COS HE II PROXIMITY ZONE SPECTRA

In our radiative transfer models, the He II proximity zone sizes were determined from high-resolution ( $dr = 11.9$  comoving kpc,  $dv = 0.86\text{--}0.93\text{ km s}^{-1}$  at  $z_{\text{em}} = 2.74\text{--}3.5$ ) noise-free He II proximity zone Ly $\alpha$  transmission spectra that had not been degraded to the spectral resolution and quality of the actual *HST*/COS spectra. We explored the consequences of this simplification with fully forward-modelled mock *HST*/COS He II proximity zone spectra of two quasars from our sample (Q 1602+576 taken with the G130M grating and SDSS J1253+6817 taken with the G140L grating), analogously to Worseck et al. (2016, 2019). For twelve different combinations of initial He II fraction  $x_{\text{HeII},0} \in \{0.01, 0.05, 0.5, 1.0\}$  and quasar on-time  $t_{\text{on}} \in \{1, 10, 100\}$  Myr twenty model spectra were convolved with the respective *HST*/COS line-spread functions. Given the actual quasar continuum flux, grating sensitivity, exposure time, background conditions and spectral binning, expected COS counts per pixel were computed from the convolved He II transmission spectra. Realistic COS Poisson counts were simulated as Poisson deviates of the expected counts, and then converted back to He II transmission. Finally,  $R_{\text{pz}}$  was determined in the same way as for the observed spectra. Redshift error was not included here.

Figure A1 shows the observed *HST*/COS He II proximity zone spectra and representative mock spectra of Q 1602+576 and SDSS J1253+6817. We chose the combinations of  $x_{\text{HeII},0}$  and  $t_{\text{on}}$  the  $R_{\text{pz}}$  distribution of which match best the measured values. Apart from the small-scale structure in the proximity zone sourced by the density field, the mock spectra resemble the observed spectra very well. The bottom panels show the relative deviations of the proximity zone sizes determined in the mock spectra ( $R_{\text{pz}}$ ) with respect to the ones in the high-resolution noise-free model spectra ( $R_{\text{sim}}$ ). For most of the 240 mock spectra per quasar the values are very similar, in particular for the range of quasar on-times our method is sensitive to ( $t_{\text{on}} < 30$  Myr). For long quasar on-times  $t_{\text{on}} \sim 100$  Myr,  $R_{\text{pz}}$  is sometimes significantly larger than  $R_{\text{sim}}$  due to subtle deviations between the smoothed He II transmission profiles when accounting for the broad wings of the COS line-spread functions and the coarser binning of the COS spectra. In G140L spectra, proximity zone sizes  $\lesssim 5$  pMpc are overestimated by up to 10 per cent, primarily due to the sharp drop of the He II transmission profile for short quasar on-times  $\lesssim 1$  Myr. However, this bias is smaller than the error in  $R_{\text{pz}}$  induced by quasar redshift error (Table 1). For larger  $R_{\text{sim}}$  the bias

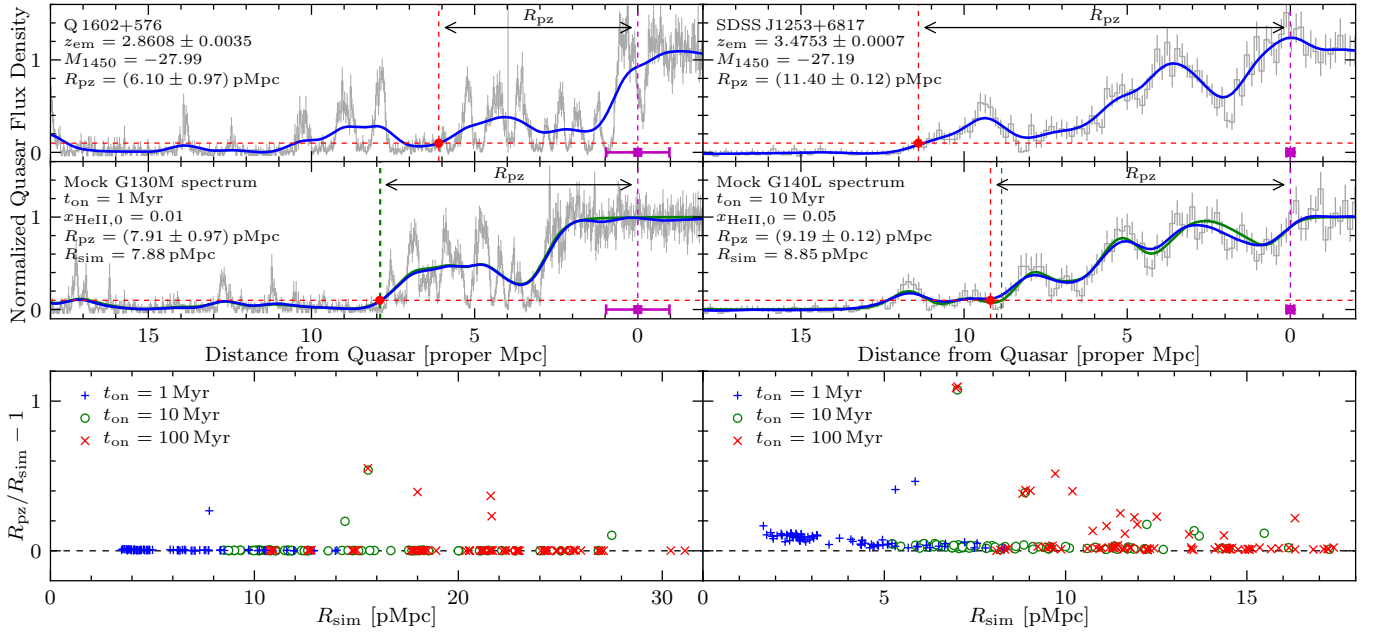


**Figure A1.** Comparison of observed *HST*/COS He II quasar proximity zone spectra (top panels, labelled) to representative realistic mock spectra (middle panels). The left (right) panels show COS G130M (G140L) spectra, plotted in grey with statistical  $1\sigma$  Poisson errors. Distances are for the He II Ly $\alpha$  transition relative to the quasar at redshift  $z_{em}$ , with negative distances indicating pixels in the quasar continuum. The violet squares with error bars mark the quasar redshift uncertainties. The blue lines show the flux smoothed with a Gaussian filter with FWHM 1 pMpc. The red dots mark the measured  $R_{pz}$ . The green solid lines in the middle panels show the smoothed high-resolution noise-free He II transmission from our radiative transfer models employed in our MCMC analysis, yielding a different proximity zone size  $R_{sim}$  (green dashed). The bottom panels show the relative deviation of  $R_{pz}$  with respect to  $R_{sim}$  in the radiative transfer models for three values of the quasar on-time  $t_{on}$  (labelled). The dashed lines mark zero deviation.

monotonically decreases to  $\lesssim 2$  per cent, as the He II proximity zone transmission profile drops more gradually. In COS G130M spectra the proximity zone size is generally not significantly overestimated even at small  $R_{sim}$ , as expected. The intrinsic scatter of  $R_{pz}$  around  $R_{sim}$  is small, i.e.  $R_{pz}$  is robustly estimated in the COS spectra used in our analysis (see the middle panels of Fig. A1). We verified the robustness of  $R_{pz}$  in the lowest-quality spectra ( $S/N \sim 3$ ).

This paper has been typeset from a  $\text{\LaTeX}$  file prepared by the author.